Nano Research 2017, 10(12): 4055–4081
DOI 10.1007/s12274-017-1671-7
Review Article

ISSN 1998-0124
CN 11-5974/O4

Phosphorus and phosphide nanomaterials for sodium-ion batteries

Qingbing Xia[1,2], Weijie Li[2], Zongcheng Miao[1] (✉), Shulei Chou[2] (✉), and Huakun Liu[2]

[1] *Key Laboratory of Organic Polymer Photoelectric Materials, School of Science, Xijing University, Xi'an 710123, China*
[2] *Institute for Superconducting and Electronic Materials, Australian Institute of Innovative Materials, University of Wollongong, North Wollongong, NSW 2500, Australia*

Received: 30 March 2017
Revised: 4 May 2017
Accepted: 7 May 2017

KEYWORDS

sodium-ion batteries,
anodes,
nanostructure,
phosphorus,
phosphides

ABSTRACT

Sodium-ion batteries have received remarkable attention as next-generation high-performance electrochemical energy storage devices because of their cost effectiveness and the broad geographical distribution of sodium. As a critical component of sodium-ion batteries, anode materials, especially nanostructured anodes, have a significant effect on the electrochemical performance of sodium-ion batteries. Recent research indicates that phosphorus and metal phosphides show great promise as anode candidates for sodium-ion batteries because of their low cost and relatively high theoretical gravimetric and volumetric specific capacities. In this review, we systematically summarize recent research progress on state-of-the-art nanostructured phosphorus and phosphides, including the synthetic strategies, Na-storage mechanisms, and the relationship between the nanostructure and electrochemical performance. Moreover, we present an overview of future challenges and opportunities based on current developments.

1 Introduction

Nowadays, novel sustainable and renewable energy sources, such as solar energy, wind energy, and geothermal power, have aroused considerable attention because of the continuous environmental degradation caused by the large-scale utilization of traditional fossil fuels. Highly efficient, environmentally friendly, and reliable electrochemical energy storage (EES) technologies are in strong demand to accelerate the use of these clean energy sources. Of the various EES technologies, lithium-ion batteries (LIBs) have shown remarkable promise and have been widely used in portable electronic devices, electric vehicles, and grid-scale energy storage owing to their high energy densities and long cycle lives [1–7]. Much of the accessible global lithium reserve is distributed in remote or politically sensitive areas [8], which pushes up the production cost of LIBs. Recently, sodium-ion batteries (SIBs) have become regarded as a potential alternative for LIBs because of their cost effectiveness and the geographical distribution of sodium. Sodium

---

Address correspondence to Zongcheng Miao, miaozongcheng@xijing.edu.cn; Shulei Chou, shulei@uow.edu.au

is the 4th most abundant element on earth, and it has a suitable redox potential of –2.71 V vs. the standard hydrogen electrode (SHE), which is only 0.3 V higher than that of lithium, meaning that SIBs are promising replacements for LIBs in large-scale applications [9–12]. Currently, one of the major challenges in SIBs is to find suitable electrode materials, especially anode materials, to improve the electrochemical characteristics, such as energy density, cycling life, and charge/discharge capability, which would promote the practical use of SIBs. Carbonaceous materials, such as disordered carbon and graphite, have been commercially utilized as the anode materials for LIBs, but, unfortunately, they are electrochemically less active in SIBs, meaning that not all the LIB anode material can be directly adopted to SIBs probably because of the larger ionic radius of the sodium ion (1.02 Å) compared to that of the lithium ion (0.76 Å) [13–19].

Recently, increasing research into novel high-performance sodium-ion storage materials, including carbonaceous materials [20, 21], metals [22–25], alloys [26–29], metal oxides [30–32], sulfides [33–35], and phosphorus and phosphides [36–40], has been carried out. Among the above-mentioned anode candidates, phosphorus and metal phosphides (MPs) have drawn significant attention because of their unique physical properties and electrochemical characteristics in EES devices (such as LIBs and supercapacitors) and electrocatalysis. As an anode material for LIBs, phosphorus can react with up to three lithium atoms to form Li_3P, giving a theoretical specific capacity of 2,596 $mA\cdot h\cdot g^{-1}$ [41–43]. When used in SIBs, phosphorus has a theoretical capacity of ~2,600 $mA\cdot h\cdot g^{-1}$, assuming the formation of Na_3P after full sodiation and the optimal insertion voltage of ~0.4 V vs. Na/Na^+. Lee et al. and Yang, et al. found that ball-milled red phosphorus/carbon nanocomposites have reversible capacities of more than 2,000 $mA\cdot h\cdot g^{-1}$ and excellent rate capabilities [36, 37]. A sandwich-structured black P/graphene nanocomposite reported by Cui's group delivered an extremely high capacity of 2,440 $mA\cdot h\cdot g^{-1}$ at 50 $mA\cdot g^{-1}$ [44]. Despite these advantages, the application of phosphorus in SIBs is handicapped by many drawbacks, such as volumetric expansion, as high as ~400%, after fully sodiation to Na_3P, which results in the pulverization and aggregation of P particles and rapid capacity fade. In addition, the low electrical conductivity of ~10^{-14} $S\cdot cm^{-1}$ also results in large polarization and sluggish kinetics. Apart from phosphorus, metal phosphides also show promise as anode materials for SIBs owing to their noticeably high gravimetric and volumetric specific capacities, appropriate redox potentials, and high electrical conductivities. For instance, Sn_4P_3 has a higher theoretical volumetric specific capacity (6,650 $mA\cdot h\cdot cm^{-3}$) than that of P (5,710 $mA\cdot h\cdot cm^{-3}$). Our group synthesized a series of MPs via mechanical ball milling, such as $Sn_{4+x}P_3$@(Sn-P), FeP, and CoP, which presented good electrochemical performance [39, 45–47]. Like P, the large volume change generated by the sodium-ion insertion-extraction processes is the major issue for MPs application in SIBs.

Because the electrochemical performance of an anode material is strongly associated with the particle size, morphology, and chemical composition, and can be enhanced by specially designed nanoarchitectures [48, 49], many novel nanostructures have been designed to buffer the volume expansion. Generally, active materials on the nanoscale can effectively reduce the ion and electron transport paths, and alleviate the mechanical stress caused by volume expansion during repeated sodiation/desodiation. Several excellent reports on the application of nanostructured phosphorus and phosphides in SIBs, such as yolk–shell Sn_4P_3 and nanowire arrays of Cu_3P, have been reported, and these materials accommodate the volume expansion well and show excellent cycling stability [50, 51].

The use of phosphorus and phosphides as the anode materials for SIBs is a hot research topic, partly because of their appealing electrochemical characteristics. In this review, we systematically summarize the recent research progress on state-of-the-art nanostructured phosphorus and phosphides, including the synthetic strategies, sodium-ion storage mechanisms, and architectures. Finally, we conclude with an overview of future challenges and opportunities based on current developments. We hope that this review will increase the understanding of phosphorus and phosphides in SIBs, aiding the future development and applications of sodium-ion batteries.

2 Nanostructured phosphorus anodes for SIBs

Phosphorus has three main allotropes: red, black, and white phosphorus. Among the allotropes, white P is chemically unstable and flammable, which makes it unsuitable for application as an electrode material for SIBs. Both amorphous and crystalline red and black phosphorus can react with sodium ions to form Na_3P, giving a theoretical capacity of ~2,600 mA·h·g^{-1}, the highest among existing SIB anodes. Table 1 summarizes the synthetic methods and electrochemical performance of different nanostructured phosphorous compositions. In this section, we will discuss the recent developments in nanostructured red P, black P, and phosphorene in relation to SIBs.

2.1 Red phosphorus (RP)

Red phosphorus has been identified as a promising anode for SIBs because of its remarkably high specific capacity and low redox potential (< 0.4 V). However, red P faces the following major challenges: a low electronic conductivity of ~10^{-14} S·cm^{-1} and large volume expansion of ~400% upon full sodiation, which seriously limit its practical application. The most effective approach to circumvent these issues is to hybridize red P with a conductive matrix, such as carbon, carbon nanotubes, or graphene, to fabricate composite nanoarchitectures, which not only enhance the conductivity of red P but also alleviate the volume expansion effectively.

2.1.1 *Red phosphorus/carbon (RP/C) composites*

Lee and coworkers carried out pioneering research in utilizing red phosphorus as an anode for SIBs, independently [37]. The authors prepared a phosphorus/carbon (P/C) composite by ball milling commercial phosphorus with super P carbon, in which the

Table 1 Summary of phosphorous nanostructures anodes in sodium-ion batteries

Nanostructure	Synthetic method	Cycling stability (after *n* cycles)	Rate capability	Ref.
RP/super P	Ball milling	143 mA·g^{-1}, ~1,800 mA·h·g^{-1}, n = 30	2.86 A·g^{-1}, 1,540 mA·h·g^{-1}	[37]
RP/super P	Ball milling	250 mA·g^{-1}, ~800 mA·h·g^{-1}, n = 140	4 A·g^{-1}, 1,715 mA·h·g^{-1}	[36]
RP/graphene scrolls	Quick-freezing	250 mA·g^{-1}, 2,172 mA·h·g^{-1}, n = 150	4 A·g^{-1}, 1,084 mA·h·g^{-1}	[53]
RP/graphene	Ball milling	1 A·g^{-1}, 649 mA·h·g^{-1}, n = 200	10 A·g^{-1}, 274 mA·h·g^{-1}	[55]
RP/graphene	Ball milling	260 mA·g^{-1}, 1,706 mA·h·g^{-1}, n = 60	5.2 A ·g^{-1}, ~520 mA·h· g^{-1}	[56]
C@RP/graphene aerogel	Vapor redistribution	2.6 A·g^{-1}, 1,095.5 mA·h·g^{-1}, n = 200	5.2 A·g^{-1}, 878.6 mA·h·g^{-1}	[52]
RP/C@graphene	Spray dried	0.1 A·g^{-1}, ~2,000 mA·h·g^{-1}, n = 100	2 A·g^{-1}, ~1,200 mA·h·g^{-1}	[54]
RP/CNTs	Hand grinding	143 mA·g^{-1}, ~750 mA·h·g^{-1}, n = 20	None	[59]
RP/SWCNTs	Vaporization condensation	2 A·g^{-1}, ~250 mA·h·g^{-1}, n = 2,000	2 A·g^{-1}, ~300 mA·h·g^{-1}	[57]
RP/CNTs/polymer binder	Ball milling	520 mA·g^{-1}, 1,586.2 mA·h·g^{-1}, n = 100	5.2 A·g^{-1}, ~850 mA·h·g^{-1}	[58]
RP@CMK-3	Vaporization- condensation-conversion	12.975 A·g^{-1}, 1,020 mA·h·g^{-1}, n = 210	25.431 A·g^{-1}, 650 mA·h·g^{-1}	[61]
RP@N-MPC	Vaporization-condensation-conversion	1 A·g^{-1}, 450 mA·h·g^{-1}, n = 1,000	9 A·g^{-1}, 291 mA·h·g^{-1}	[62]
RP-TiP_2-C	Ball milling	200 mA·g^{-1}, ~607 mA·h·g^{-1}, n = 100	800 mA·g^{-1}, ~526 mA·h·g^{-1}	[63]
RP/Sb/Cu	Ball milling	125 mA·g^{-1}, >1,100 mA·h·g^{-1}, n = 50	2 A·g^{-1}, >900 mA·h·g^{-1}	[64]
BP/Ketjenblack-MWCNTs	Ball milling	1.3 A·g^{-1}, 1,700 mA·h·g^{-1}, n = 100	3 A·g^{-1}, 928 mA·h·g^{-1}	[72]
PN/graphene	Self-assembly	26 A·g^{-1}, ~500 mA·h·g^{-1}, n = 100	26 A·g^{-1}, 645 mA·h·g^{-1}	[44]

Abbreviations are as follows: RP = red phosphorous, BP = black phosphorous, PN = phosphorene, CNTs = carbon nanotubes, SWCNTs = single walled carbon nanotubes, MWCNTs = multi walled carbon nanotubes, CMK-3 = mesoporous carbon, and N-MPC = nitrogen-doped microporous carbon.

amorphous particles were uniformly mixed with the carbon at the nanoscale, which could well accommodate the volume expansion. The P/C composite had a low redox potential of ~0.4 V vs. Na/Na$^+$ and exhibited a considerable reversible capacity of 1,890 mA·h·g^{-1} when used with a poly(acrylic acid) (PAA) binder, Furthermore, the composite had a stable cycling performance with less than 7% capacity fade after 30 cycles (Figs. 1(a) and 1(b)). In addition, the composite also presented an excellent rate capability, delivering ~1,540 mA·h·g^{-1} even at a current density of 2.86 A·g^{-1}. *Ex situ* X-ray diffraction (XRD) revealed that the amorphous red phosphorus was transformed into a Na_3P phase after full electrochemical reduction (Fig. 1(c)). Independently, Yang's group also reported a ball-milled amorphous red phosphorus/carbon (a-P/C) nanocomposite as an anode material for SIBs [36]. The a-P/C nanocomposite had a high Na$^+$ storage capacity of 1,764 mA·h·g^{-1}. When tested in 10% fluoroethylene carbonate (FEC) containing an electrolyte, the composite maintained a capacity of approximately 1,000 mA·h·g^{-1} after 80 cycles, and this remained constant for 140 cycles (Fig. 1(d)).

2.1.2 *Red phosphorus/graphene (RP/G) composites*

Graphene, which has a high surface area, flexibility, and high conductivity, has been introduced as a matrix to improve the electrical conductivity and accommodate the volume changes of phosphorus [52–56]. For example, Pei et al. [53] encapsulated nanosized red phosphorus particles in graphene scrolls to form a phosphorus-graphene (P-G) composite (Fig. 2(a)). This well-designed rolled graphene provides an interconnected conductive network and restrains the volume expansion and aggregation of P particles during the sodiation/desodiation processes. The as prepared P-G composite with a 50.8% phosphorus content delivered an extremely high reversible capacity of 2,355 mA·h·g^{-1} and maintained an excellent cycling performance with a capacity retention of 92.3% (2,172 mA·h·g^{-1} capacity) over 150 cycles at 250 mA·g^{-1}. The performance decayed rapidly, however, at a high

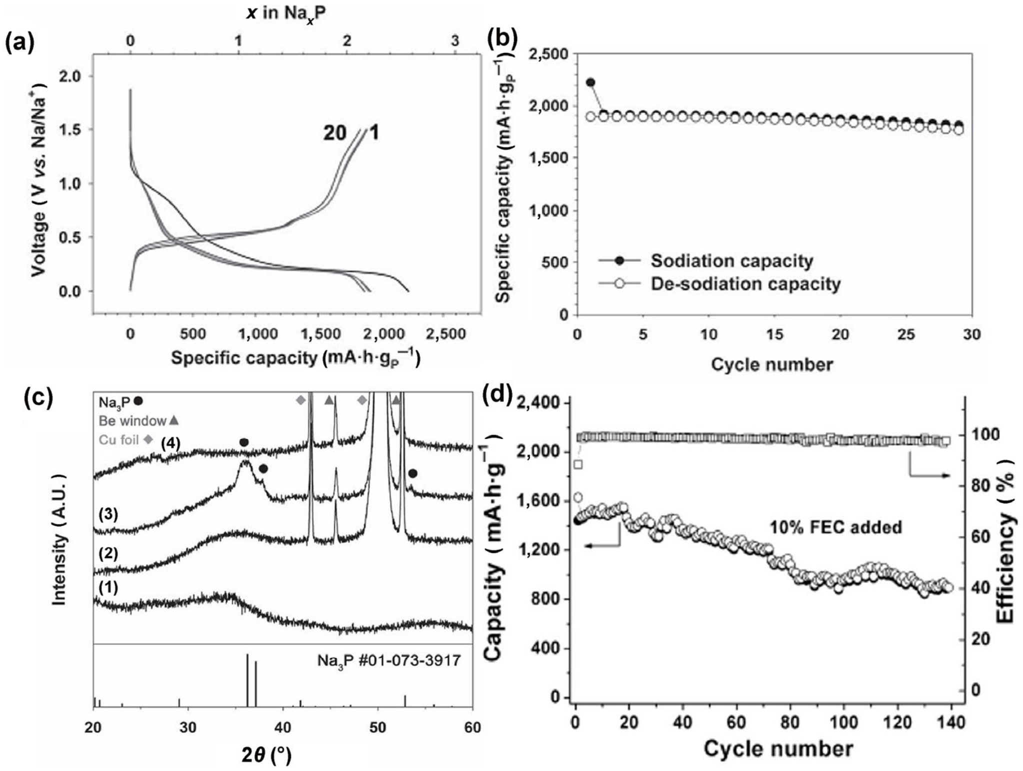

Figure 1 (a) Voltage profiles and (b) cycling performance of an amorphous red P/C composite containing a PAA binder. (c) *Ex situ* XRD patterns of an amorphous red P/C composite electrodes at different discharge/charge states. Reproduced with permission from Ref. [37], © 2013 WILEY-VCH Verlag GmbH & Co. KGaA, Weinheim. (d) Cycling performance of a-P/C composite in 10% fluoroethylene carbonate containing the electrolyte. Reproduced with permission from Ref. [36], © 2013 WILEY-VCH Verlag GmbH & Co. KGaA, Weinheim.

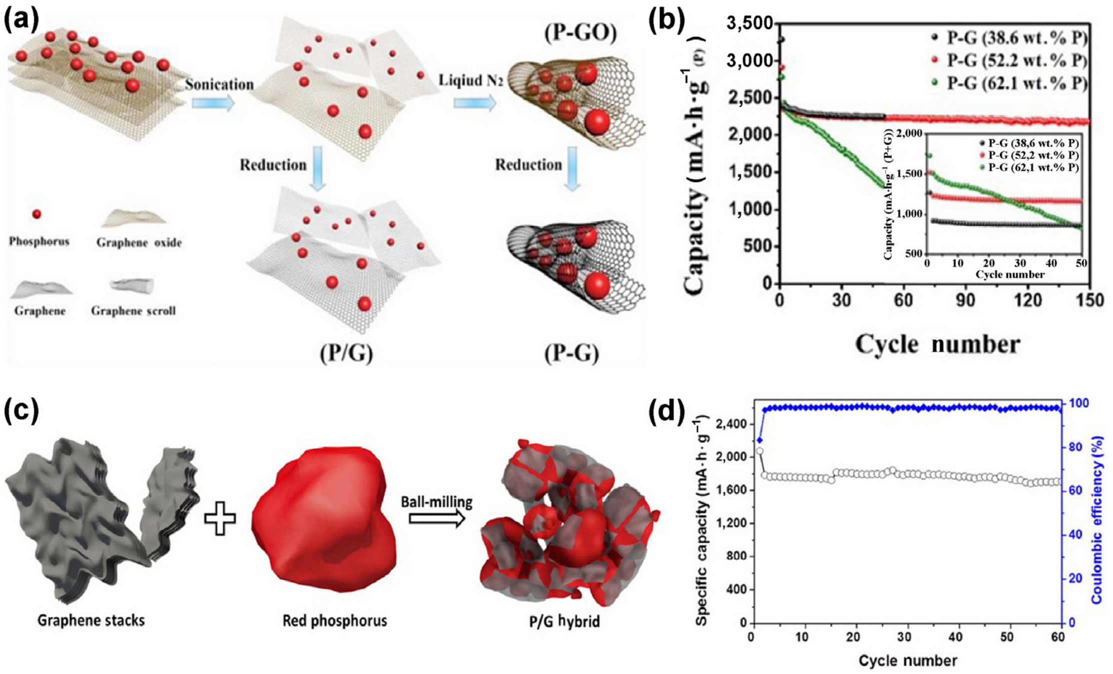

Figure 2 (a) Schematic illustration of the preparation of P-graphene (G) and P/G composites. (b) Cycling performance of the P-G composites with different P contents. Reproduced with permission from Ref. [53], © 2015 Wiley-VCH Verlag GmbH & Co. KGaA, Weinheim. (c) Schematic illustration of the synthesis of P/G nanosheet hybrids. (d) Cycling stability and coulombic efficiency of the P/G hybrid anode at a current density of 260 mA·g^{-1}. Reproduced with permission from Ref. [56], © 2014 American Chemical Society.

P mass loading (62.1%), as shown in Fig. 2(b). Our group reported a phosphorus/graphene nanoplates composite (P/GnP) through the ball milling of commercial red phosphorus and natural graphite [55]. The graphite was exfoliated into graphene nanoplates by shear forces, and the exfoliated graphene nanoplates were chemically bonded with P particles so that they acted as a conductive network to buffer the volume change in the P particles. When tested as an anode for SIBs, this P/GnP composite showed stable cycling capability with 92.5% capacity retention after 200 cycles at 1 A·g^{-1} current density; furthermore, even at the 10 A·g^{-1} rate, it still achieved a capacity of 274 mA·h·g^{-1}. Song and coworkers [56] also developed a chemically bonded phosphorus/graphene hybrid through ball milling. The exfoliated graphene nanosheets were in intimate contact with the P particles via P-O-C bonds, which is beneficial for enhancing the electrical conductivity and stabilizing the solid electrolyte interphase (SEI) film upon large volume expansion during repeated cycling (Fig. 2(c)). The hybrid presented an initial capacity of 2,077 mA·h·g^{-1} and maintained a cycling capacity of 1,700 mA·h·g^{-1} with 95% capacity retention over 60 cycles (Fig. 2(d)).

Aside from the traditional ball-milling method, new techniques have been developed to synthesize red P/C composites. A 3D interacting carbon-coated red P/graphene aerogel (C@P/GA) nanoarchitecture fabricated via a vapor-redistribution strategy has been reported by Gao et al. [52]. The synthesis process includes two steps, as illustrated in Fig. 3(a): an *in situ* self-assembly process to encapsulate the red P into a 3D graphene matrix to form P/GA, and polypyrrole, which is used as a vapor carbon source, to localize the P nanoparticles (C@P/GA). This well-designed C@P/GA composite is quite different from other P/graphene hybrids [55, 56], in which the nanosized (10–20 nm) P particles are uniformly distributed and tightly sealed in the C@GA 3D matrix (Fig. 3(b)). The C@GA matrix can effectively suppress the aggregation of P nanoparticles and accommodate the volume variations during cycling, as well as provide a conductive framework to facilitate electron transfer. When tested at the 1 C rate, the C@P/GA hybrid displayed a stable cycling performance with a capacity of 1,095.5 mA·h·g^{-1}, which was retained over 200 cycles (Fig. 3(c)).

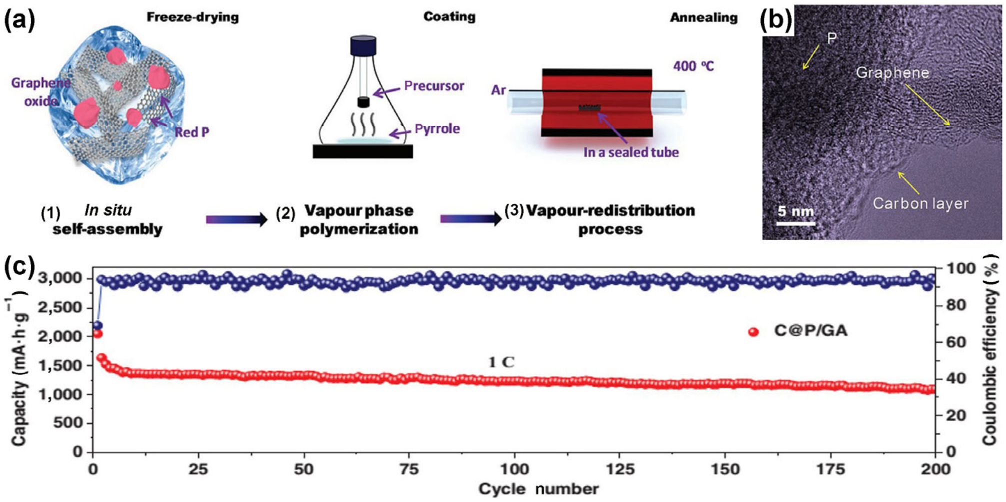

Figure 3 (a) Schematic illustration of the synthesis process for the C@P/GA composite. (b) High-resolution transmission electron microscope (HRTEM) image of C@P/GA. (c) Cycling performance of C@P/GA composite at 1 C (1 C = 2,600 mA·g^{-1}). Reproduced with permission from Ref. [52], © 2016 WILEY-VCH Verlag GmbH & Co. KGaA, Weinheim.

2.1.3 *Red phosphorus/carbon nanotube (RP/CNT) composites*

Carbon nanotubes (CNTs) have also been used as a promising conductive network to modify the performance of battery materials because of their highly electronically conductive characteristics and outstanding mechanical properties [57–60]. Our group fabricated a P/CNT composite by simply hand grinding commercial microsized red P and CNTs [59]. The P/CNT composite exhibited unexpectedly high sodium-ion storage capability and delivered an initial discharge capacity of 2,210 mA·h·g^{-1}, which is much higher than that of commercial red phosphorus (~1,600 mA·h·g^{-1}). The cycling capacity decayed rapidly, however, retaining only 76.6% capacity after 10 cycles. Zhu and coworkers reported a phosphorus-single-wall carbon nanotube (P-SWCNT) composite synthesized via a vaporization-condensation method [57]. The red P particles were well dispersed between tangled SWCNT bundles and intimately attached to the SWCNTs. The highly conductive and mechanically strong SWCNT skeleton ensured the high electronic conductivity of the composite but also contributed to forming a stable interface between the electrolyte and the P particles, alleviating the stress induced by the Na$^+$ intercalation/de-intercalation. The P-SWCNT composite exhibited an excellent rate capability with a capacity of ~300 mA·h·g^{-1} at a current density of 2,000 mA·g^{-1}. The long-term cycling capability was much improved with 80% capacity retention after 2,000 cycles at a cycling current density of 2,000 mA·g^{-1}.

To maintain the structural stability of red phosphorus in the electrochemical process, Song et al. adopted a multiple bonding strategy to chemically bond the red P, carbon nanotubes functionalized with carboxylic acid groups, and a cross-linked polymer binder, sodium carboxymethylcellulose citric acid (NaCMC-CA) to form a 3D network, a P/CNT/NaCMC-CA composite anode [58]. The P/CNT hybrid was firstly synthesized by ball milling commercial red P and carboxylic-group-functionalized CNTs. The mechanical force resulted in the formation of strong P–O–C bonds between the red P particles and the CNTs during ball milling; then, the P/CNT hybrid was further chemically bonded with the cross-linked carboxymethyl cellulose-citric acid binder to form a robust electrode, as shown in Figs. 4(a) and 4(b). In contrast to the conventional phosphorus anode designs, in this P/CNT/NaCMC-CA composite, the P–O–C bonds link the red phosphorus particles intimately with the conducting carbon network composed of CNTs, increasing the durability of the red P particles. On the other hand, the cross-linked binder forms a 3D network chemically bonded with the CNTs to form a robust electrode. This chemical bonding strategy shows a significant improvement in suppressing the volume changes and

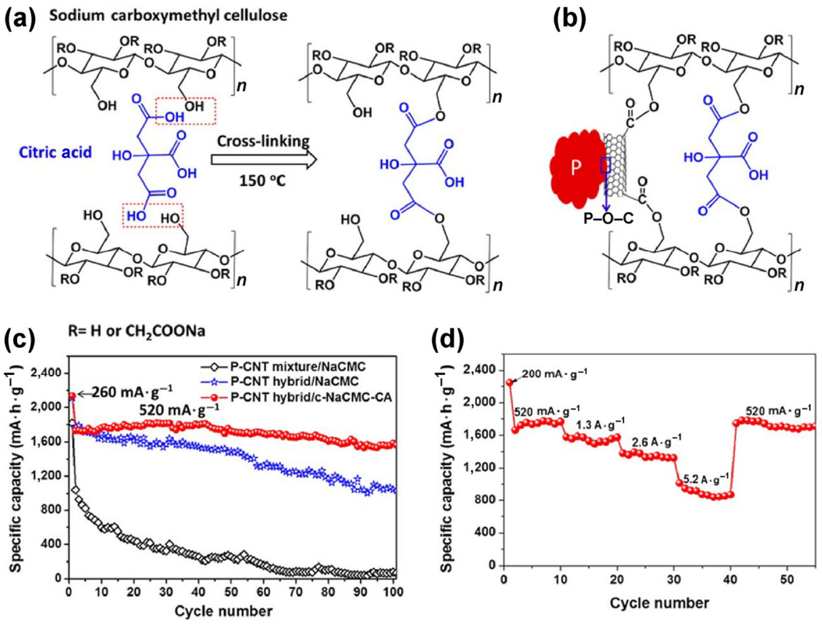

Figure 4 (a) Schematic illustration of the synthesis of a sodium carboxymethyl cellulose and citric acid (c-NaCMC-CA) cross-linked polymer binder. (b) The interaction between the P-CNT hybrid and c-NaCMC-CA binder. (c) Cycling stability and (d) rate performance of P-CNT hybrid/c-NaCMC-CA electrode. Reproduced with permission from Ref. [58], © 2015 American Chemical Society.

maintaining the structural stability of the red P particles during the sodiation/desodiation processes. Benefiting from these advantages, this P/CNT/NaCMC-CA robust anode delivered an initial reversible capacity as high as 2,134.7 mA·h·g^{-1}, with a high coulombic efficiency of 84.7%, and presented good cycling performance with a capacity of 1,586.2 mA·h·g^{-1}, which was retained after 100 cycles at a current density of 520 mA·g^{-1} (Fig. 4(c)). The rate capability was also significantly improved, and, even at a cycling current density of 5.2 A·g^{-1}, and a high reversible specific capacity of ~850 mA·h·g^{-1} (Fig. 4(d)) was achieved.

2.1.4 Other red phosphorus/conductive matrix composites

Other types of conductive matrices, such as mesoporous carbon [61], N-doped microporous carbon [62], transition metal phosphides [63], and transition metals [64], have also been utilized to relieve the volumetric variation of P during electrochemical processes. A nanocomposite of red P particles confined in a mesoporous carbon matrix (P@CMK-3) was reported by Yu's group [61], where the confinement was achieved via the vaporization-condensation-conversion method. They analyzed the Li^{+} and Na^{+} storage capability of the composite (Fig. 5(a)) and found that this unique structure has a variety of advantages. For example, open ionic migration channels and high electronic conductivity are offered by CMK-3, and the intimate contact between the nanosized P particles and CMK-3 suppresses the growth and agglomeration of red P nanoparticles. As an anode material for SIBs, P@CMK-3 displayed a high specific capacity of 2,594 mA·h·g^{-1} (based on the mass of red P) and a reversible capacity of 1,020 mA·h·g^{-1} (based on the mass of red P) over 210 cycles at the 5 C cycling rate (Fig. 5(b)). Apart from mesoporous carbon, Yu's group also developed a metal-organic framework (MOF)-derived N-doped microporous carbon to improve the sodium-ion storage performance of red P [62]. The sub-nanometer size red P particles were homogenously encapsulated in a zeolitic imidazolate framework (ZIF-8) derived N-doped microporous carbon matrix (P@N-MPC) via the vaporization-condensation-conversion method. A schematic illustration of the synthesis is presented in Fig. 5(c). The P@N-MPC composite with a porous structure and completely inherited the polyhedron-like morphology of ZIF-8. The resulting unique structure has various advantages:

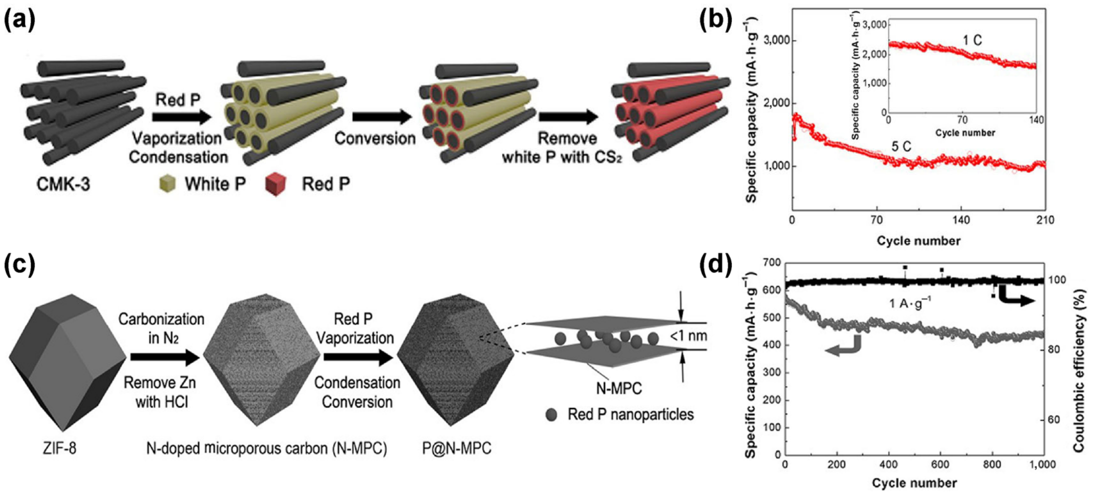

Figure 5 (a) Schematic illustration of the preparation process for the P@CMK-3 material. (b) Cycling performance of P@CMK-3 at 1 and 5 C rates. Reproduced with permission from Ref. [61], © 2016 American Chemical Society. (c) Schematic illustration of the preparation process for P@N-microporous carbon (MPC). (d) Cycling performance of P@N-MPC composite at 1 A·g^{-1}. Reproduced with permission from Ref. [62], © 2017 WILEY-VCH Verlag GmbH & Co. KGaA, Weinheim.

The highly porous N-MPC matrix can suppress the huge volume expansion of red P nanoparticles during charge/discharge processes. Furthermore, the sub-1 nm micropores ensure efficient access of the electrolyte to the red P particles, enhancing the electrochemical activity. In addition, the carbon matrix contains highly conductive pathways for electrons to improve the conductivity of the red P nanoparticles. The composite presented a reversible capacity of ~600 mA·h·g^{-1} at 0.15 A·g^{-1}, and superior cycling over 1,000 cycles at a cycling current density of 1 A·g^{-1} with an extremely low capacity fading rate of 0.02% per cycle (Fig. 5(d)).

In addition, transition metal phosphides have also been applied as buffer materials. For instance, Kim et al. [63] reported a P-TiP$_2$-C composite and found that the crystalline TiP$_2$ phase in combination with carbon played a crucial role in maintaining the structural stability of the red P particles during cycling, resulting a relatively stable cyclability with 80.4% capacity retention (~607 mA·h·g^{-1}) after 100 cycles. However, the reversible capacity was significantly lower than for other P/carbon-based composites.

2.2 Black phosphorus (BP)

Compared with other allotropes (red phosphorus and white phosphorus), black phosphorus is the least reactive. However, it has much higher electrical conductivity [65, 66]. Black phosphorus has a layered structure like that of graphite but the interlayer distance much larger than that of graphite (5.4 vs. 3.4 Å) [67–69]. The larger interlayer distance enables sodium ions to intercalate/remove into/from the layer structure easily. Orthorhombic black phosphorus with a layered crystal structure is the most thermodynamically stable of the phosphorous allotropes [70, 71].

Most recently, black P has attracted much attention as anode material for lithium-/sodium-ion batteries because it has an electrical conductivity as high as 300 S·m^{-1}, a large interlayer spacing, and a high theoretical specific capacity [41, 72–74]. Computational studies have been performed to understand the diffusion of Na atoms in black P, and the results indicate that sodium ions undergo a planar intercalation mechanism and can easily intercalate into the interlayer spaces of black P, preferring to localize in the same layers to form a composition of Na$_{0.25}$P on further sodiation; this results in an alloying process that is accompanied by the breaking of P–P bonds, large volume expansion, and the eventual formation of an amorphous phase, Na$_x$P [75, 76]. Experimental characterization showed that the incomplete transformation of black P to the Na$_3$P phase in the sodiation process results in a lower reversible capacity; the large volume variation caused the active materials to gradually disintegrate and delaminate from the current collectors, leading to capacity deterioration during cycling [77].

Xu et al. [72] fabricated a black P/Ketjen-black-multiwalled carbon nanotube (BPC) composite by high energy ball milling for use as an anode material for SIBs. The nanosized black phosphorus particles were homogeneously distributed in the carbon matrix (Fig. 6(a)). The as-prepared BPC composite displayed a first-cycle reversible capacity of 2,011.1 mA·h·g^{-1} with a coulombic efficiency of 91.1% and excellent cycling performance, demonstrating a high capacity of 1,700 mA·h·g^{-1} over 100 cycles at 1.3 A·g^{-1}. When tested under a high current density of 3 A·g^{-1}, the composite showed a discharge capacity of 928 mA·h·g^{-1}, an excellent rate capacity. *In situ* synchrotron high-energy X-ray diffraction (HEXRD), small/wide-angle X-ray scattering (S/WAXS) and nuclear magnetic resonance (NMR) revealed the multi-step sodiation/desodiation mechanism. In the discharge process, the black phosphorus particles were first transformed to an amorphous NaP intermediate, followed by a crystalline Na_3P phase after further sodiation. During the subsequent desodiation process, the crystalline Na_3P phase gradually converted back to amorphous phosphorus with a small amount of amorphous NaP remaining in the electrode (Figs. 6(b)–6(d)), thus resulting in excellent electrochemical performance.

2.3 Phosphorene (PN)

Phosphorene, which consists of either a monolayer or a few layers of black phosphorus, has been studied as a new 2d layered material. Composed of individual layers held together by Van der Waals interactions, phosphorene possesses a layered structure with in-plane anisotropy and a puckered honeycomb structure, which shares structural similarity with graphene, as shown in Figs. 7(a) and 7(b) [65, 66, 78, 79]. Recent studies have revealed that the bandgap of phosphorene can be tuned from 0.33 to 2.0 eV as a function of layer number, giving a wide range of ultrafast electron transfer kinetics [80–83]. Because of its unique properties, phosphorene has attracted significant attention and is considered a promising material for use in transistors [84, 85], photodetectors [86–88], and photovoltaics [89, 90]. Previous reports have shown

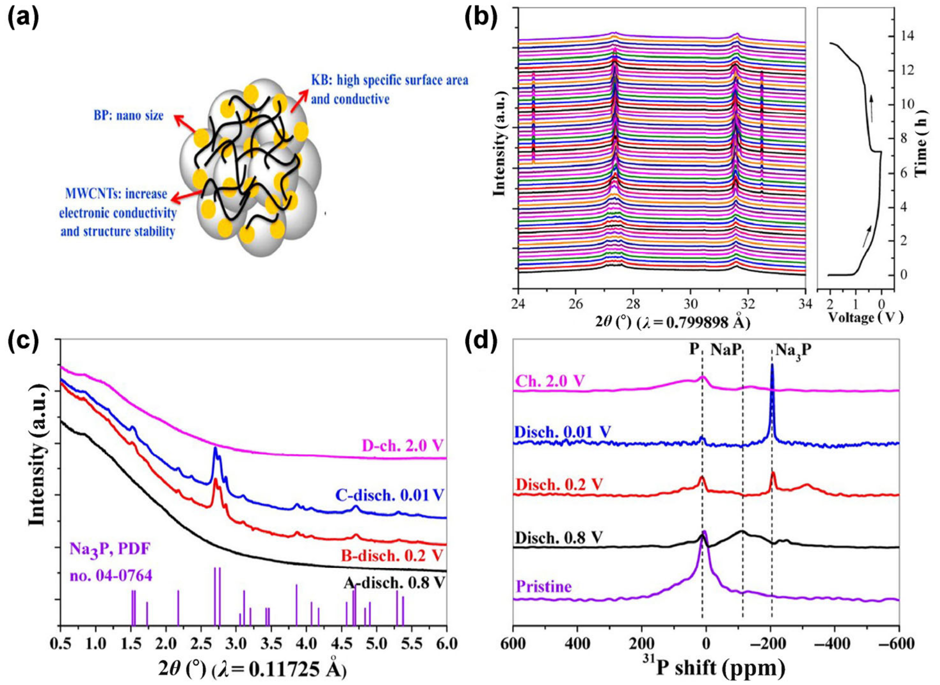

Figure 6 (a) Schematic illustration of the structure of BPC composite. (b) *In situ* HEXRD patterns in the first cycle at 0.1 C of BPC anode. (c) *Ex situ* HEXRD patterns and (d) ^{31}P-NMR spectra of BPC anode at different charge/discharge states. Reproduced with permission from Ref. [72], © 2016 American Chemical Society.

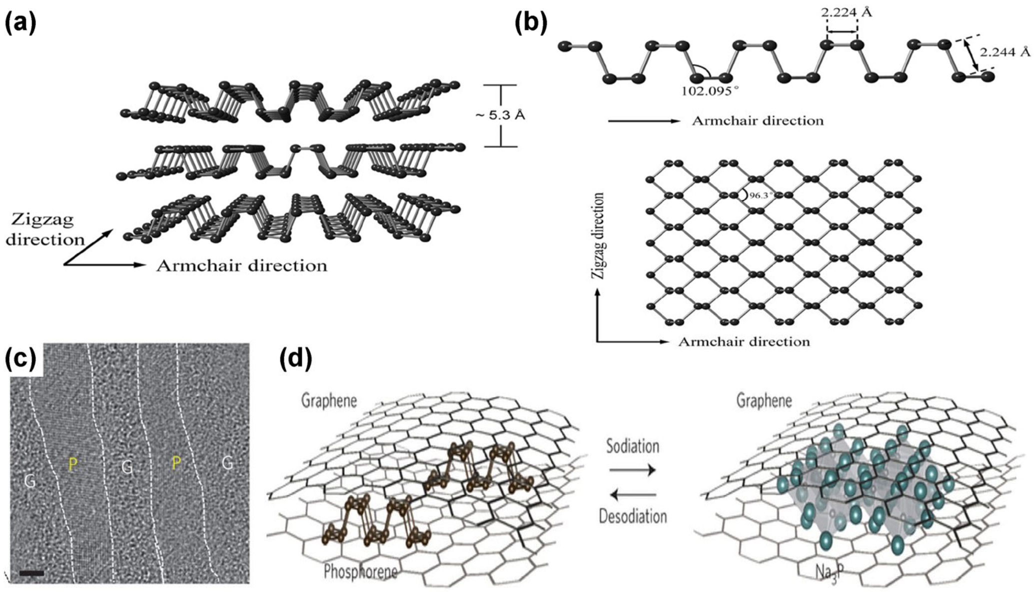

Figure 7 (a) Atomic structure of multi-layer black phosphorus and (b) monolayer phosphorene. Reproduced with permission from Ref. [78], © 2015 the Royal Society of Chemistry. (c) HRTEM image of the phosphorene–graphene hybrid. (d) Structural evolution of the sandwiched phosphorene–graphene structure during sodiation. Reproduced with permission from Ref. [44], © 2015 Macmillan Publishers Limited.

that 2D-layered phosphorene can be successfully used as an anode for lithium-ion batteries, where it achieves excellent electrochemical performance [91, 92]. Although there have been only a few reports concerning phosphorene in SIBs, phosphorene shows great promise as a SIB anode material.

First principles studies indicate that sodium ions can be stabilized on the surface of phosphorene and have a very low diffusion energy barrier (only ~0.04 eV), indicating the high mobility of sodium ions during the charge/discharge processes [80, 81]. Nie et al. [93] used *in situ* transmission electron microscopy (TEM) and density functional theory (DFT) to study the selective diffusion behavior of sodium ions in phosphorene. They found that sodium ions prefer to diffuse along the [100] direction in both few-layer and monolayer phosphorene. The DFT calculations revealed that the zigzag edge of phosphorene provides faster diffusion paths for the sodium ions in comparison to the armchair edges and surfaces. These theoretical studies indicate the immense potential of phosphorene as anode material for SIBs. So far there have been a few reports in the literature concerning the applications of phosphorene in SIBs. Cui's group [44] reported a phosphorene-graphene hybrid with a few phosphorene layers sandwiched between graphene layers, as shown in Fig. 7(c). *In situ* TEM and *ex situ* X-ray diffraction revealed a two-step sodiation mechanism. In the first step, sodium ions insert themselves into the phosphorene interlayers along the *x*-axis, followed by alloying with phosphorene to form a Na_3P phase. For the sandwiched phosphorene-graphene hybrid, the graphene layers provide an elastic buffer space to accommodate the anisotropic volumetric expansion of phosphorene layers along the *y*- and *z*-axial directions during the sodiation process (Fig. 7(d)). The hybrid shows a reversible capacity of 2,440 $mA \cdot h \cdot g^{-1}$ at 0.05 $A \cdot g^{-1}$ and maintains an 83% capacity retention over 100 cycles. Furthermore, even when tested at 26 $A \cdot g^{-1}$, the hybrid maintained a capacity retention of 77% after 100 cycles.

3 Nanostructured metal phosphides (MPs) in SIBs

Phosphorus-based metal phosphides, such as Sn-P [38–40, 50, 94], Fe-P [45, 46, 95, 96], Co-P [47, 97–99], and Cu-P [51, 100, 101] alloys have been investigated as anode materials for SIBs because of their relatively low intercalation potentials vs. Na/Na^+ and high theoretical gravimetric and volumetric energy densities compared with hard carbon, metal oxides, and metal sulfides [19, 30, 102–104], demonstrating their potential as promising anodes for high-performance sodium-ion batteries. The various metal phosphides that have been applied in SIBs are described in Table 2. However, metal phosphides suffer from remarkable capacity fading during repeated cycling, principally owing to the poor charge transfer kinetics and the huge volumetric expansion, which results in the pulverization and aggregation of active materials. Many promising approaches have been used to solve this problem, such as combining metal phosphides with conductive matrices [38, 94, 105] and fabricating core/yolk-shell nanostructures [39, 50, 98] and nanowire arrays [51].

3.1 Synthetic strategies

The synthetic methods for nanostructured metal phosphides to be applied in SIBs can be generally divided into three categories: mechanical ball milling [38–40, 45–47, 96, 100, 101, 106–109], solution phase [50, 94, 97, 110, 111], and gas-solid phase methods [51, 95, 98, 99].

3.1.1 *Mechanical ball-milling method*

As a cost-effective, environmentally friendly, and large-scale production method, mechanical ball milling has been widely applied to the synthesis of a variety of nanostructured electrode materials for LIBs and SIBs. The mechanical ball-milling strategy can effectively break down the bulk materials, e.g., red P and metals,

Table 2 Summary of the preparation of various nanostructured metal phosphide anodes in sodium-ion batteries

Type of material	P source	Synthetic method	Cycling stability (after *n* cycles)	Rate capability	Ref.
Sn_4P_3	RP	Ball milling	$100\ mA\cdot g^{-1}$, $\sim600\ mA\cdot h\cdot g^{-1}$, $n = 100$	None	[40]
Sn_4P_3/Carbon	RP	Ball milling	$100\ mA\cdot g^{-1}$, $\sim500\ mA\cdot h\cdot g^{-1}$, $n = 150$	$1\ A\cdot g^{-1}$, $349\ mA\cdot h\cdot g^{-1}$	[38]
$Sn_{4+x}P_3$@(Sn-P) core–shell structure	RP	Ball milling	$100\ mA\cdot g^{-1}$, $465\ mA\cdot h\cdot g^{-1}$, $n = 100$	$10\ A\cdot g^{-1}$, $58.2\ mA\cdot h\cdot g^{-1}$	[39]
Sn_4P_3@carbon yolk–shell nanospheres	RP	Solution phase	$1.5\ A\cdot g^{-1}$, $360\ mA\cdot h\cdot g^{-1}$, $n = 400$	$3\ A\cdot g^{-1}$, $421\ mA\cdot h\cdot g^{-1}$	[50]
Sn_4P_3/graphene	RP	Solution phase	$1\ A\cdot g^{-1}$, $362\ mA\cdot h\cdot g^{-1}$, $n = 1{,}500$	$2\ A\cdot g^{-1}$, $391\ mA\cdot h\cdot g^{-1}$	[94]
Sn_4P_3	WP	Solution phase	$50\ mA\cdot g^{-1}$, $305\ mA\cdot h\cdot g^{-1}$, $n = 10$	None	[110]
SnP_3	RP	Ball milling	$150\ mA\cdot g^{-1}$, $\sim810\ mA\cdot h\cdot g^{-1}$, $n = 150$	$2{,}560\ mA\cdot g^{-1}$, $\sim400\ mA\cdot h\cdot g^{-1}$	[106]
FeP	RP	Ball milling	$50\ mA\cdot g^{-1}$, $321\ mA\cdot h\cdot g^{-1}$, $n = 60$	None	[45]
FeP/graphite	RP	Ball milling	$50\ mA\cdot g^{-1}$, $175\ mA\cdot h\cdot g^{-1}$, $n = 70$	$2.5\ A\cdot g^{-1}$, $56\ mA\cdot h\cdot g^{-1}$	[46]
CNT@FeP@C	NaH_2PO_2	Gas-solid phase	$500\ mA\cdot g^{-1}$, $295\ mA\cdot h\cdot g^{-1}$, $n = 500$	$1.5\ A\cdot g^{-1}$, $268\ mA\cdot h\cdot g^{-1}$	[95]
Graphene@CoP@FeP core–shell structure	NaH_2PO_2	Gas-solid phase	$100\ mA\cdot g^{-1}$, $456.2\ mA\cdot h\cdot g^{-1}$, $n = 200$	$2\ A\cdot g^{-1}$, $341.2\ mA\cdot h\cdot g^{-1}$	[99]
CoP	RP	Ball milling	$100\ mA\cdot g^{-1}$, $315\ mA\cdot h\cdot g^{-1}$, $n = 25$	$2A\cdot g^{-1}$, $80\ mA\cdot h\cdot g^{-1}$	[47]
1D CoP/Carbon	TOPO	Solution phase	$4.467\ A\cdot g^{-1}$, $\sim300\ mA\cdot h\cdot g^{-1}$, $n = 1{,}000$	$4.467\ A\cdot g^{-1}$, $314.84\ mA\cdot h\cdot g^{-1}$	[97]
CoP@carbon/graphene-Nickel foam core–shell structure	$NaH_2PO_2\cdot H_2O$	Gas-solid phase	$100\ mA\cdot g^{-1}$, $473.1\ mA\cdot h\cdot g^{-1}$, $n = 100$	$1.6\ A\cdot g^{-1}$, $155\ mA\cdot h\cdot g^{-1}$	[98]
Ni_2P/graphene 3D yolk–shell-like structure	$NiNH_4PO_4\cdot H_2O$	Solid annealing	$0.2\ A\cdot g^{-1}$, $181\ mA\cdot h\cdot g^{-1}$, $n = 100$	$2\ A\cdot g^{-1}$, $101\ mA\cdot h\cdot g^{-1}$	[105]
Cu_3P nanowires	NaH_2PO_2	Gas-solid phase	$1\ A\cdot g^{-1}$, $133.8\ mA\cdot h\cdot g^{-1}$, $n = 260$	$5\ A\cdot g^{-1}$, $137.8\ mA\cdot h\cdot g^{-1}$	[51]
CuP_2/carbon	RP	Ball milling	$150\ mA\cdot g^{-1}$, $\sim430\ mA\cdot h\cdot g^{-1}$, $n = 30$	$2\ A\cdot g^{-1}$, $178\ mA\cdot h\cdot g^{-1}$	[100]
CuP_2/carbon	RP	Ball milling	$200\ mA\cdot g^{-1}$, $\sim450\ mA\cdot h\cdot g^{-1}$, $n = 100$	$800\ mA\cdot g^{-1}$, $308\ mA\cdot h\cdot g^{-1}$	[101]

Abbreviations are as follows: RP = red phosphorous, WP = white phosphorous, and TOPO = trioctylphosphine oxide.

into well-mixed microscale or nanoscale particles to accelerate the alloying process. We have succeeded in synthesizing $Sn_{4+x}P_3$@(Sn-P), FeP, FeP/graphite, and CoP nanocomposites as anode materials for SIBs by mechanically ball milling commercial red P with the corresponding metallic material, and the products demonstrate good electrochemical performance [39, 45–47]. In the $Sn_{4+x}P_3$@(Sn-P) composite, the Sn_4P_3 nanoparticle has a core–shell structure with the core having an average size of 30 nm surrounded by a 3 nm thick amorphous layer of Sn-P alloy, as shown in Fig. 8(a). Mechanical ball milling can easily yield different phases by regulating the proportions of the components. For instance, Fan et al. prepared P-rich phosphide SnP_3/C composite by simply ball milling Sn, red P, and carbon black [106].

3.1.2 *Solution phase method*

Compared with the traditional ball-milling method, the solution phase method, like the solvothermal method, is effective for synthesizing phosphides with high phase purity, high crystallinity, and controllable morphologies and size distributions. Yu's group reported yolk–shell Sn_4P_3@C nanospheres synthesized via a low-temperature solvothermal phosphorization process using yolk-shell Sn@C nanospheres as reaction templates and red P as the phosphorus source. The as-prepared nanostructure exhibited a morphology inherited from the Sn@C nanospheres (Fig. 8(b)) [50]. Li et al. used a similar solution phosphorization process to synthesize a Sn_4P_3/ reduced graphene oxide (rGO) composite having a hybrid nanoarchitecture with Sn_4P_3 nanoparticles (~6 nm) homogeneously loaded onto the rGO nanosheets [94]. Yan's group synthesized a one-dimensional (1D) carbon-supported nanostructured CoP and FeP_4 through an oil-phase route, with self-assembled amphiphilic fibrous elastin proteins serving as starting materials and templates (Fig. 8(c)). The 1D CoP and FeP_4 materials were composed of nanosized particles decorated on carbon supports, which were ~2 μm in length and 5–10 nm in diameter. The 1D CoP nanostructures presented excellent electrochemical

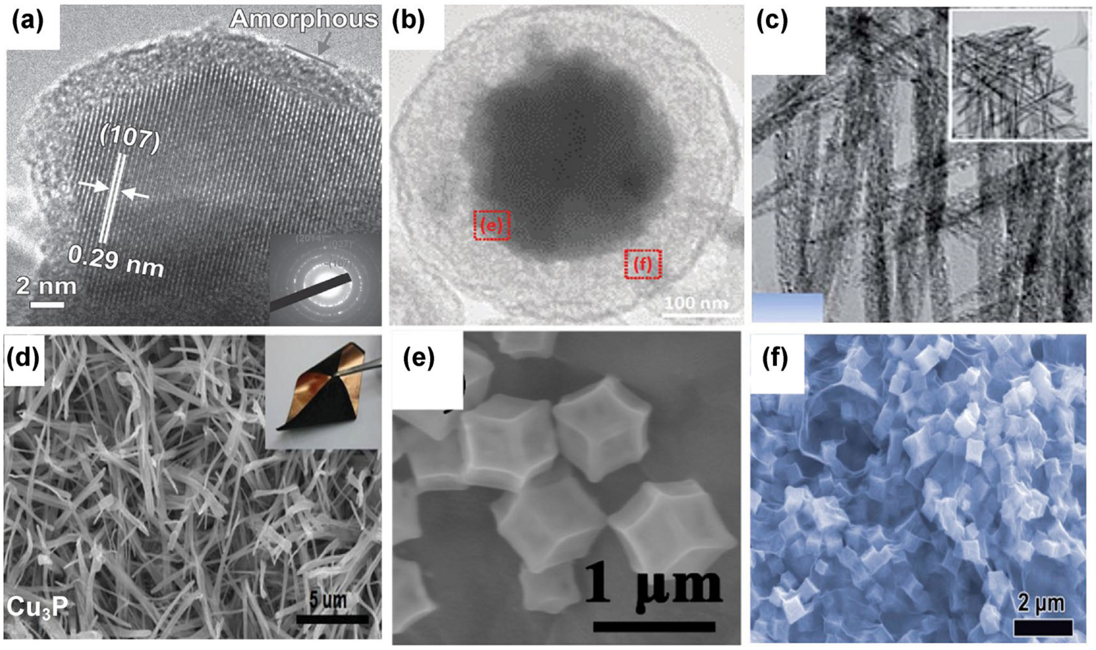

Figure 8 (a) HRTEM images of $Sn_{4+x}P_3$@(Sn-P) composite. Reproduced with permission from Ref. [39], © 2014 WILEY-VCH Verlag GmbH & Co. KGaA, Weinheim. (b) TEM images of the yolk–shell Sn_4P_3@C nanospheres. Reproduced with permission from Ref. [50], © 2015 the Royal Society of Chemistry. (c) TEM image of the 1D CoP nanostructures. Reproduced with permission from Ref. [97], © 2016 the Royal Society of Chemistry. (d) Cu_3P nanowire array. Reproduced with permission from Ref. [51], © 2016 WILEY-VCH Verlag GmbH & Co. KGaA, Weinheim. (e) SEM image of CoP@C-rGO-NF nanostructure. Reproduced with permission from Ref. [98], © 2016 Elsevier Ltd. (f) SEM images of the rGO@CoP@FeP composite. Reproduced with permission from Ref. [99], © 2017 Elsevier Ltd.

performance both in LIBs and SIBs [97].

3.1.3 *Gas–solid-phase method*

The reported solid phase processes have mainly focused on using phosphine (PH_3) as the phosphorus source and reductant for the *in situ* phosphorizations of metal oxides, hydroxides, and metal organic frameworks into metal phosphides. Phosphine is easily generated from sodium hypophosphite at a low temperature (over 250 °C). Fan et al. reported a binder-free Cu_3P nanowire-array anode grown on copper foil by the *in situ* phosphorization of a $Cu(OH)_2$ nanowire array using PH_3, which was produced by the decomposition of NaH_2PO_2 (Fig. 8(d)) [51]. Yin's group used PH_3 as a reductant with phosphorus for the phosphorization of metal organic frameworks, e.g., ZIF-67 and $Co(OH)_2$@PB, to obtain core–shell CoP@C polyhedrons and core–shell CoP/FeP porous microcubes (Figs. 8(e) and 8(f)), which inherit the precursor morphology and dimensions and achieve good electrochemical performances [98, 99]. However, PH_3 is extremely toxic and lethal in low concentrations (ppm), so extreme care is needed to operate the reaction process and dispose of the reaction tail gas.

3.2 Na-storage mechanism

In general, metal phosphides have sodium-ion storage mechanisms based on the electrochemical conversion reaction, as in lithium-ion batteries. Compared with the intercalation reaction mechanism, more electrons can participate in the electrochemical conversion reaction mechanism, resulting in much higher specific capacities. For tin phosphides, e.g., Sn_4P_3 and SnP_3, both the Sn and the P components can further react with sodium ions to form alloys, thereby contributing to the capacity, when used as anodes for SIBs. For some metal phosphides, such as FeP [45] and CoP [47, 98], the insertion of sodium ions in the first discharge process is usually accompanied by the destruction of phosphorus–metal bonds, leading to the direct formation of nanosized metallic nanocrystals and an Na_xP phase. The nanosized metallic nanocrystals serve as highly conductive electronic channels, enabling fast charge transfer kinetics, and an elastic matrix to buffer the huge volumetric expansion of P during the subsequent sodium-ion insertion/deinsertion processes. The corresponding reaction process can be proposed:

$$MP_x + 3xNa^+ + 3xe^- \rightarrow xNa_3P + M \tag{1}$$

$$Na_3P \leftrightarrow 3Na^+ + P + 3e^- \tag{2}$$

Other phosphides, such as CuP_2 [100, 101], Cu_3P [51], and NiP_3 [109], experience a reversible conversion reaction mechanism, as shown in Eq. (3), with minor differences from those of FeP and CoP, in which the metallic phases formed after the full sodiation alloys with P, converting back to phosphide phases after full desodiation.

$$MP_x + 3xNa^+ + 3xe^- \leftrightarrow xNa_3P + M \tag{3}$$

Sn_4P_3, however, undergoes a combined conversion reaction and alloying-dealloying mechanism [38, 39, 50, 94]. During the initial sodiation process, Sn_4P_3 decomposes into $Na_{15}Sn_4$ and Na_3P phases (Eq. (4)). Sodium ions are extracted from $Na_{15}Sn_4$ and Na_3P phases to form metallic Sn and P nanocrystals in the subsequent desodiation process. In the subsequent cycles, Sn and P particles alloy/de-alloy with sodium ions to jointly provide capacity (Eq. (5) and Eq. (6)). According to this combined reaction mechanism, Sn_4P_3 can accommodate up to 24 sodium ions, indicating a theoretical specific capacity of 1,132 $mA \cdot h \cdot g^{-1}$.

$$Sn_4P_3 + 24Na^+ + 24e^- \rightarrow Na_{15}Sn_4 + 3Na_3P \tag{4}$$

$$Na_{15}Sn_4 \leftrightarrow 4Sn + 15Na^+ + 15e^- \tag{5}$$

$$Na_3P \leftrightarrow 3Na^+ + P + 3e^- \tag{6}$$

However, research into metal phosphide anode materials for SIBs is still in the early stages, and much work and new analytical techniques are needed to understand the Na-storage mechanisms.

3.3 Tin phosphide materials

Tin phosphide (Sn_4P_3) has attracted special attention as an anode material for SIBs because of its high theoretical capacity (1,132 $mA \cdot h \cdot g^{-1}$), high theoretical volumetric specific capacity (6,650 $mA \cdot h \cdot cm^{-3}$), high electrical conductivity (30.7 $S \cdot cm^{-1}$), and low redox potential (0.3 V vs. Na/Na^+) [25, 38–40, 50, 94, 108, 110, 111]. Like red phosphorus and metallic Sn anodes, tin phosphides also suffer from large volume variation during the charge/discharge processes [25, 38–40]. Kim et al. [40] first studied the sodium-ion storage behavior of Sn_4P_3. Their ball-milled Sn_4P_3 delivered a reversible capacity of 718 $mA\cdot h\cdot g^{-1}$ and a stable cycling performance with almost no capacity fading over 100 cycles when tested in an electrolyte with added FEC (Fig. 9(a)). Qian et al. [38] reported a Sn_4P_3/C nanocomposite synthesized through the ball-milling method as an anode for SIBs. The as-prepared nanocomposite demonstrated a high sodium-ion storage capacity of 850 $mA\cdot h\cdot g^{-1}$ at 50 $mA\cdot g^{-1}$ and considerable cycling stability, with 86% capacity retention after 150 cycles at a current density of 0.1 $A\cdot g^{-1}$, which is far beyond those of P/C and Sn/C composites (Fig. 9(b)). The authors attributed the excellent performance to the synergistic Na-storage mechanism of the initial products, P and metallic Sn. The uniform distribution of nanosized Sn particles enables the electrochemical activation of the P component, while the P particles and their discharge product Na_3P serve as a shielding matrix to alleviate the aggregation of Sn particles and suppress their volume expansion during the sodium insertion process, as illustrated in Fig. 9(c). Our group [39] fabricated a $Sn_{4+x}P_3$@(Sn-P) nanocomposite with a core–shell structure using low-speed ball milling. As shown in Fig. 8(a), the $Sn_{4+x}P_3$ component has a particle size of 30 nm with an amorphous Sn-P composite layer covering the surface. When used as anode for SIBs, the as-prepared composite with a carboxymethyl cellulose binder delivered a reversible capacity of 892 $mA\cdot h\cdot g^{-1}$ at 100 $mA\cdot g^{-1}$, and the cycling stability was significantly enhanced, having a capacity retention of 92.6% (calculated at the 2nd cycle) after 100 cycles when 5 vol.% was FEC added to the electrolyte (Fig. 9(d)).

Recently, novel nanoarchitectures have been proposed

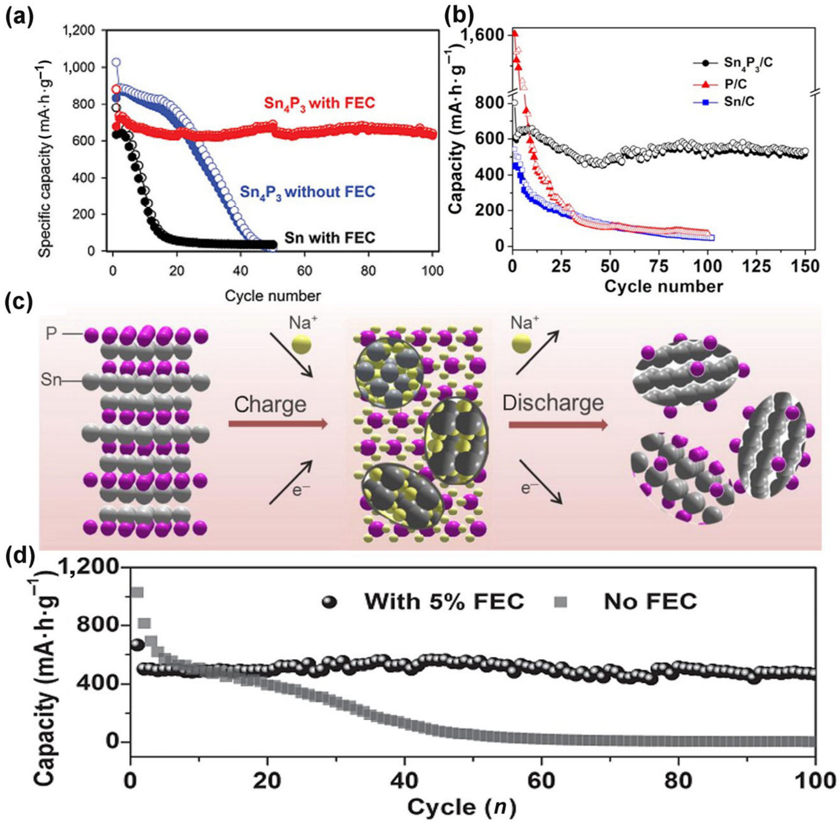

Figure 9 (a) Cycling performance of Sn_4P_3 and Sn electrodes obtained with or without added FEC. Reproduced with permission from Ref. [40], © 2014 WILEY-VCH Verlag GmbH & Co. KGaA, Weinheim. (b) Comparison of the reversible capacities of the Sn_4P_3/C, Sn/C, and P/C electrodes at a current rate of 100 $mA\cdot g^{-1}$. (c) Schematic illustration of the Na-storage mechanism in the Sn_4P_3 electrode. Reproduced with permission from Ref. [38], © 2014 American Chemical Society. (d) Cycling performance of $Sn_{4+x}P_3$@(Sn-P) composite at a current density of 100 $mA\cdot g^{-1}$. Reproduced with permission from Ref. [39], © 2014 WILEY-VCH Verlag GmbH & Co. KGaA, Weinheim.

to solve the volume expansion problem. Yolk–shell nanostructures have been widely used to buffer the volume variation of the electrode materials during the charge/discharge processes [112–116]. For instance, Yu's group [50] designed a yolk–shell Sn_4P_3@C nanosphere through a top-down phosphorization route, as illustrated in Fig. 10(a). The synthesis process can generally be divided into two parts: the synthesis of yolk–shell Sn@C nanospheres precursors and the conversion of the yolk–shell Sn@C into yolk–shell Sn_4P_3@C nanospheres via solvothermal phosphorization. In this unique structure, the Sn_4P_3 nanoparticles are thoroughly encapsulated in uniform carbon shells (Fig. 10(b)). The yolk–shell structure offers distinct advantages in accommodating the volumetric expansion and preserving the structural integrity of the active materials during the charge/discharge process owing to the defined internal void space. When used as the anode for SIBs, this yolk–shell structured Sn_4P_3@C showed a reversible capacity as high as 790 mA·h·g^{-1}

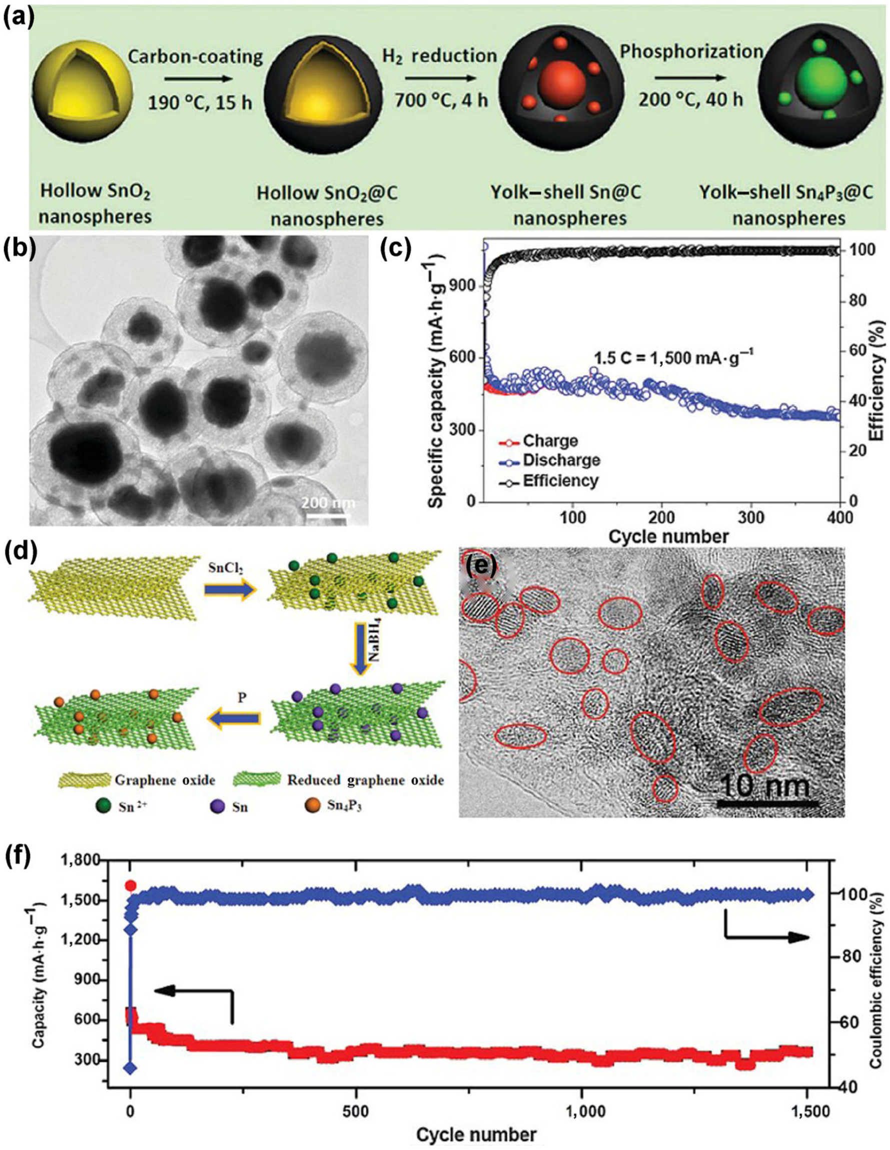

Figure 10 (a) Schematic illustration of the fabrication of uniform yolk–shell Sn_4P_3@C nanospheres. (b) TEM images of the yolk–shell Sn_4P_3@C nanospheres. (c) Cycling performance of the yolk–shell Sn_4P_3@C nanospheres at 1,500 mA·g^{-1}. Reproduced with permission from Ref. [50], © 2015 the Royal Society of Chemistry. (d) Schematic illustration of the synthesis process for the Sn_4P_3/rGO hybrid sample. (e) HRTEM image of Sn_4P_3/rGO hybrid. (f) Cycling performance of Sn_4P_3/rGO at a current density of 1.0 A·g^{-1}. Reproduced with permission from Ref. [94], © 2016 WILEY-VCH Verlag GmbH & Co. KGaA, Weinheim.

and displayed excellent cycling stability, having a capacity of 360 mA·h·g^{-1} after 400 cycles at a current density of 1,500 mA·g^{-1}. These excellent characteristics arise from the unique structural characteristics (Fig. 10(c)). Other forms of nanostructured Sn_4P_3 have been combined with reduced graphene oxide nanosheets to form a Sn_4P_3/rGO nanocomposite via a low-temperature solution-based phosphorization reaction route [94] (Fig. 10(d)), similar to Yu's work [50]. The monodisperse Sn_4P_3 nanoparticles with an average size of 6 nm were well distributed on the rGO nanosheets (Fig. 10(e)), which interconnect to form a 3D mesoporous architecture. Both the porous structure and the rGO nanosheets offer an elastic buffer to alleviate the volume expansion of Sn_4P_3 during the sodiation/desodiation process. On the other hand, the rGO nanosheets provide fast conductive pathways for electrons on the surfaces of the Sn_4P_3 nanoparticles. The synergistic effect of Sn_4P_3 and rGO significantly enhances the long-term cycling stability and rate capability, so the hybrid can maintain a high reversible capacity of 362 mA·h·g^{-1} over 1,500 cycles at 1 A·g^{-1} and a remarkable rate capability of 391 mA·h·g^{-1}, even at higher rate of 2.0 A·g^{-1} (Fig. 10(f)).

Apart from Sn_4P_3, phosphorus-rich tin phosphide has also been reported as an anode for SIBs because P has a much higher capacity than Sn. Wang's group [106] synthesized a phosphorus-rich tin phosphide, SnP_3 with a phosphorous content of 44% wt.%, much higher than that of Sn_4P_3 (16 wt.%), giving a larger theoretical specific capacity of 1,616 mA·h·g^{-1}. The phosphorus-rich SnP_3 maintains a reversible capacity of ~810 mA·h·g^{-1} without decay over 150 cycles at a current density of 150 mA·g^{-1} and achieves a capacity of ~400 mA·h·g^{-1}, even at a charge/discharge current density of 2,560 mA·g^{-1}. The authors proposed an interesting reversible conversion reaction self-healing mechanism to illustrate the reaction process, as shown in Fig. 11. In the initial sodiation stage, SnP_3 decomposes to form nanometric metallic Sn particles through the conversion reaction (Eq. (7)). The Sn particles subsequently alloy with sodium ions to form $Na_{15}Sn_4$ upon further sodiation (Eq. (8)); unfortunately, this is usually accompanied by the pulverization and aggregation of the Sn particles. In the following desodiation process, the sodium ions are dealloyed from $Na_{15}Sn_4$ to form Sn nanocrystals and recombined with the phosphorous that has dealloyed from Na_3P, thus converting back to SnP_3. The reversible conversion reaction can heal the cracks formed in the Sn induced by the alloying process and protect the Sn particles from aggregation, thus improving the cycling life.

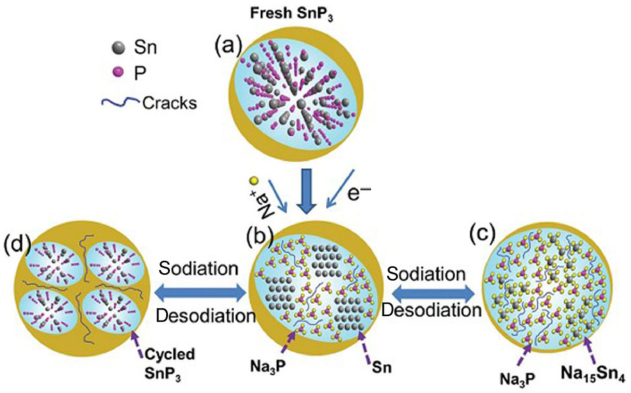

Figure 11 Schematic illustration of the sodiation and desodiation of SnP_3/C composite. Reproduced with permission from Ref. [105], © 2015 WILEY-VCH Verlag GmbH & Co. KGaA, Weinheim.

$$SnP_3 + 9Na^+ + 9e^- \leftrightarrow Sn + 3Na_3P \quad (7)$$

$$4Sn + 15Na^+ + 15e^- \leftrightarrow Na_{15}Sn_4 \quad (8)$$

3.4 Iron phosphide materials

Recently, iron phosphides (FeP, FeP_2, and FeP_4) have been investigated as anode materials for SIBs because of the high abundance, low cost, and environmentally friendly nature of Fe, which can be used as a conductive matrix to relieve the volumetric expansion of P [45, 46, 95, 96]. We have [45, 46] prepared FeP and FeP/graphite composites through ball milling and investigated their sodium-ion storage capabilities. The obtained FeP exhibited an initial reversible capacity of 460 mA·h·g^{-1} at a current density of 50 mA·g^{-1} and maintained a capacity of 321 mA·h·g^{-1} with a capacity retention of 69% (based on the 2nd cycle) over 60 cycles when CMC/PAA was used as binder and 5% FEC was added to the electrolyte. *Ex situ* XRD and TEM indicated that FeP decomposed to Fe and P after the first charge/discharge process, and the Fe acts as a conductive matrix to accommodate the volume variation in the subsequent cycles. Han et al. [95] constructed a CNT@FeP@C nanocomposite via a nanoconfinement reaction strategy. The as-prepared hierarchical nanostructure fully utilized the advantages of the amorphous and mesoporous FeP, highly conductive framework, and protective carbon layer, so that the cycling performance was much improved with a capacity retention of 90% over 500 cycles at 500 mA·g^{-1}. The novel nanostructure can be exploited to improve the electrochemical performance of FeP, for instance, rGO@CoP@FeP microcubes with CoP-coated porous FeP@C anchored on rGO nanosheets, as shown in Fig. 12(a) [99]. The Prussian-blue derived FeP microcube cores, which have an average size of 400 nm, are composed of FeP@C nanoparticles that contain abundant pores. Both the FeP core and the CoP shells react with sodium ions and contribute capacity. In addition, the pores in the FeP core and the carbon coating layer, as well as the rGO nanosheets, can easily accommodate the volume expansion during the sodiation/desodiation processes (Figs. 8(f) and 12(b)). Moreover, the carbon coating layer and rGO nanosheets together form a highly conductive network, enhancing the charge transfer kinetics. This unique microstructure benefits from the synergistic effects of each component, so the electrochemical performance of FeP was remarkably improved. The as-prepared rGO@CoP@FeP composite showed an initial reversible capacity of 551.4 mA·h·g^{-1}, which was maintained at 456.2 mA·h·g^{-1} over 200 cycles. Even when cycled at a high current density of 2 A·g^{-1}, a capacity of 341.2 mA·h·g^{-1} was achieved, which is much higher than those of CoP@C-Fe and C-Fe, demonstrating the excellent electrochemical performance of the rGO@CoP@FeP composite (Figs. 12(c) and 12(d)).

In addition, P-rich iron phosphides also show potential as anode materials for SIBs. Zhang and coworkers [96] reported the P-rich iron phosphides FeP_2 and FeP_4 that were synthesized by ball milling.

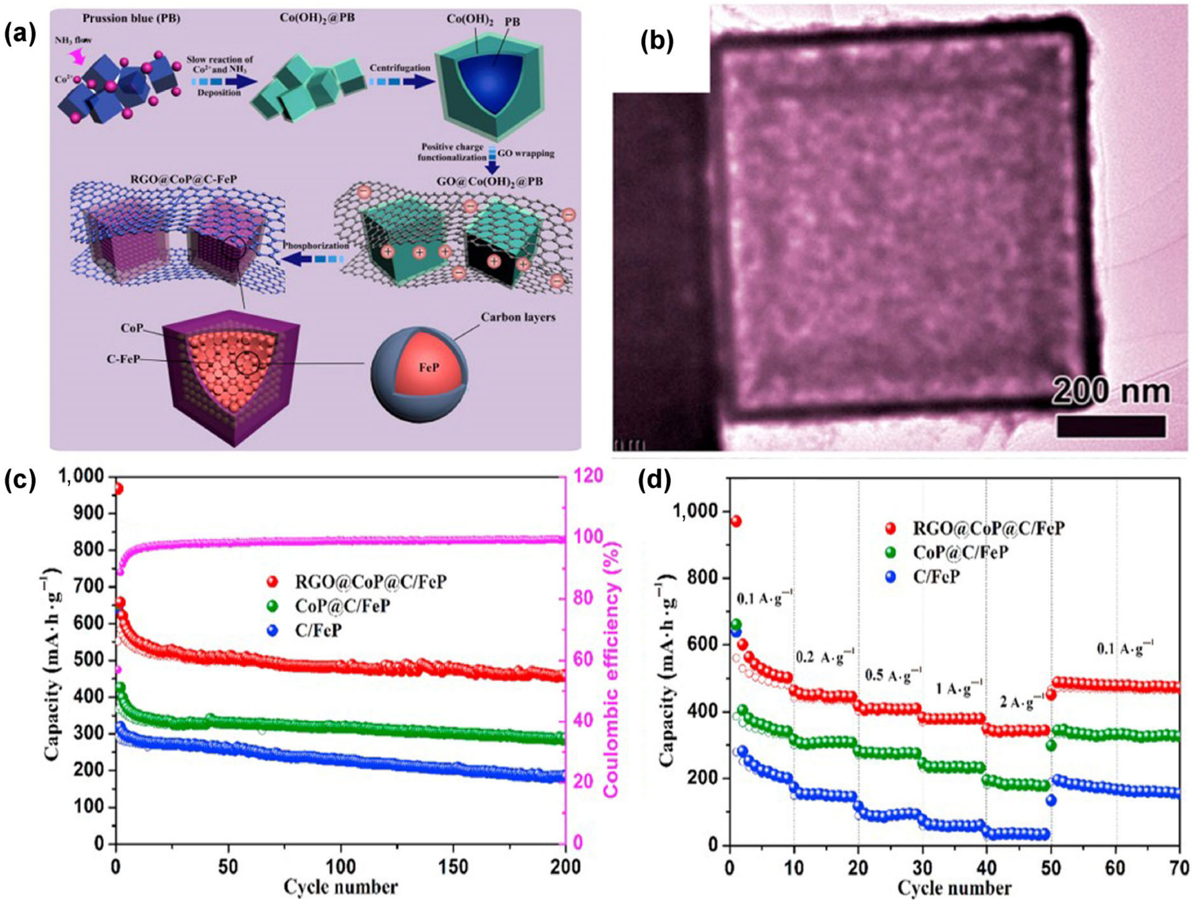

Figure 12 (a) Schematic illustration of the formation of core–shell structured rGO@CoP@C-FeP porous microcubes. (b) TEM image of a core–shell structured CoP@FeP microcube. (c) Cycling performance and (d) rate capability of the rGO@CoP@C-FeP, CoP@C-FeP, and C-FeP electrodes. Reproduced with permission from Ref. [99], © 2017 Elsevier Ltd.

FeP_2 exhibited almost no electrochemical reactivity with Na, which is unlike its behavior in LIBs [117]. However, FeP_4, displayed a reversible capacity of 1,137 mA·h·g^{-1}, corresponding to an 84% coulombic efficiency in the first cycle and maintained a stable capacity around 1,000 mA·h·g^{-1} over 30 cycles, demonstrating its promise as an anode material for sodium-ion batteries. However, the sodium-ion storage mechanism of FeP_4 is still unclear.

3.5 Cobalt phosphide materials

We have [47] synthesized cobalt phosphide (CoP) through ball-milling and found that it has a similar sodium-ion storage mechanism to that of FeP. The as-prepared CoP exhibited a high initial reversible capacity of 770 mA·h·g^{-1}, demonstrating itself to be an anode candidate for SIBs. Unfortunately, the CoP still suffers from fast capacity fading during cycling, with only 70% capacity retention (based on the 2nd cycle) after 25 cycles because of the drastic volume changes. To enhance the sodium-ion storage performance of CoP, the preparation of various smart structures, such as carbon supported 1D nanostructured CoP [97] and core–shell CoP@C-rGO nanocomposites [98], have been reported. Yin's group [98] developed a core–shell CoP@C-rGO-NF nanostructure as a binder-free anode for SIBs by using the ZIF-67 MOF as the reactant template, as illustrated in Fig. 13(a). After a low-temperature solid phosphorization process, the ZIF-67 was transformed *in situ* into porous core–shell structured CoP@C, which inherited the polyhedron morphology of ZIF-67. The MOF-derived CoP@C polyhedrons, with a 10 nm CoP core, were homogeneously anchored on the surfaces of the rGO nanosheets (Fig. 13(b)). In this unique hybrid, the carbon shell and rGO nanosheets provide adequate space to alleviate the large volume variation caused by the insertion/deinsertion of sodium ions to maintain the structural integrity of the CoP nanoparticles. On the other hand, the 3D rGO networks ensure fast electron transport pathways to enhance the charge transfer kinetics. Thus, this binder-free anode displayed remarkable cycling stability with a capacity of 473.1 mA·h·g^{-1} over 100 cycles at a current density of 100 mA·g^{-1} (Fig. 13(c)).

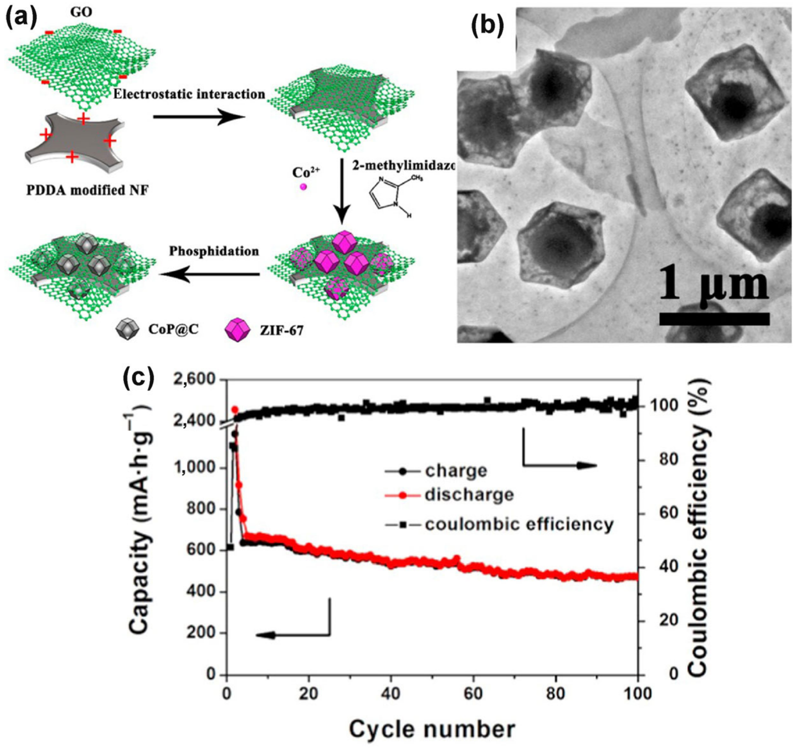

Figure 13 (a) Schematic illustration of the synthesis process for CoP@C-RGO-NF. (b) TEM image of CoP@C-RGO. (c) Cycling performance and coulombic efficiency at a current density of 100 mA·g^{-1}. Reproduced with permission from Ref. [98], © 2016 Elsevier Ltd.

3.6 Nickel phosphide materials

Nickel phosphides, Ni_2P and NiP_3, also show promise as SIB anodes [105, 109]. Yu's group [105] reported a 3D composite with yolk-shell-like Ni_2P nanoparticles embedded in porous graphene networks ($Ni_2P\subset$pGN) through an assembly and self-templating strategy, and they studied the lithium and sodium-ion storage properties of these nanoparticles. The synthesis mainly involved two steps, as shown in Fig. 14(a). In this process, the assembled nanosized $NiNH_4PO_4\cdot H_2O$ nanorods, an intermediate product, were mixed with GO nanosheets and annealed to obtain Ni_2P nanocrystals. During the annealing in an Ar/H_2 atmosphere, the nanosize $NiNH_4PO_4\cdot H_2O$ nanorods decomposed into Ni_2P nanoparticles with an average diameter of ~24 nm, which were uniformly embedded in the 3D graphene network and surrounded by many void spaces resulting from the volume contraction and cracking of the $NiNH_4PO_4\cdot H_2O$ (Fig. 14(b)). The void spaces and graphene networks provided enough space to accommodate the volume variation of Ni_2P, which resulted in structural stability during cycling. When tested as an anode for SIBs, the nickel phosphide delivered a reversible initial capacity of 214 $mA\cdot h\cdot g^{-1}$ and maintained a capacity retention of 89% over 100 cycles at 0.2 $A\cdot g^{-1}$ (Fig. 14(c)).

Fullenwarth et al. [109] reported a promising phosphorus-rich phosphide NiP_3 and found that it exhibited good sodium-ion storage behavior. The voltage profiles showed that it has a relatively low redox potential (~0.2 V vs. Na/Na^+), which is beneficial for improving the safety and energy density of SIBs. The obtained NiP_3 delivered a high initial reversible capacity (1,022 $mA\cdot h\cdot g^{-1}$). *In situ* XRD analysis indicated that the Ni_3P was directly transformed into Na_3P and nanosized metallic Ni particles via a conversion reaction with Na after full discharge and was converted into an amorphous phase in the following charge process.

3.7 Copper phosphide materials

Fan et al. [51] reported a binder-free Cu_3P nanowire array (CPNW) anode synthesized by *in situ* phosphidation of $Cu(OH)_2$ nanowires. The CPNWs with an average length of about 5 μm and diameters below 200 nm shortened the transport paths for electrons and sodium ions (Fig. 8(d)). In addition, the nanowire array anode without a binding additive provided sufficient void space to accommodate the volume expansion. As a result, the as-prepared CPNWs exhibited a high initial reversible capacity of 349 $mA\cdot h\cdot g^{-1}$ at 50 $mA\cdot g^{-1}$ and a high cycling stability, with only

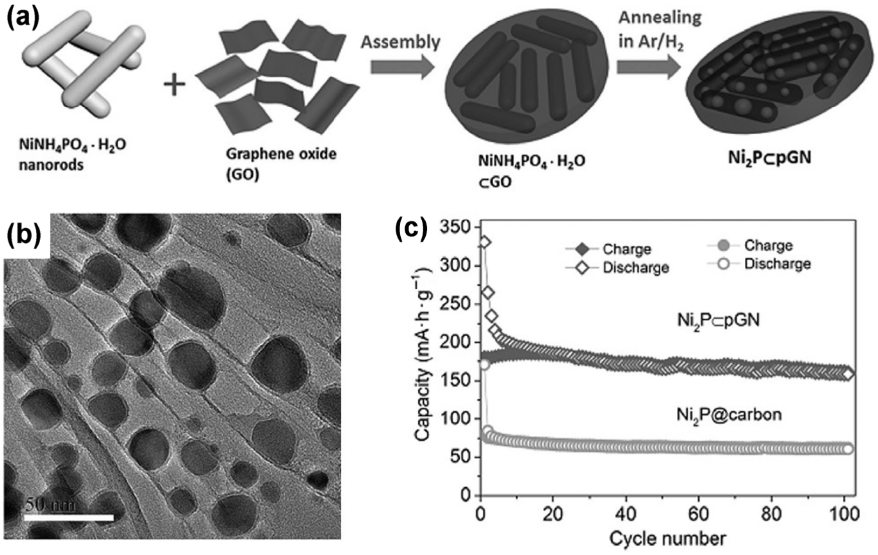

Figure 14 (a) Schematic illustration of the fabrication process for $Ni_2P\subset$pGN. (b) TEM images of $Ni_2P\subset$pGN. (c) Cycling performance of the $Ni_2P\subset$pGN and Ni_2P@carbon electrodes at 0.2 $A\cdot g^{-1}$. Reproduced with permission from Ref. [105], © 2016 WILEY-VCH Verlag GmbH & Co. KGaA, Weinheim.

0.12% capacity fade per cycle over 260 cycles at a current density of 1,000 mA·g^{-1}.

The P-rich copper phosphide CuP_2 has also been exploited as anode material for SIBs [100, 101]. Kim et al. [101] synthesized a CuP_2/C hybrid via ball milling. In this hybrid, the active CuP_2 particles were bonded into the carbon matrix by stable P–O–C chemical bonds, resulting in excellent cycling stability with 95.5% capacity retention (~450 mA·h·g^{-1}) after 100 cycles. Zhao et al. [100] also used a ball-milling process for producing a CuP_2/C nanocomposite, which could deliver a large capacity of more than 500 mA·h·g^{-1} and high rate performance.

4 Non-transition-metal phosphide materials

Apart from metal phosphides, non-metal phosphides, such as Se_4P_4 and SiP_2, also show unexpected sodium-ion storage properties [118, 119]. Chen's group developed a novel Se_4P_4 composite, which could react with 20 sodium ions, providing a theoretical capacity of 1,217 mA·h·g^{-1}. The prepared amorphous Se_4P_4 possesses much higher electrical conductivity, up to 10^{-4} S·cm^{-1}, and superior sodium-ion storage performance compared to both P and Se. The synergetic Na-storage reaction of the Se and P components in Se_4P_4 contributed a reversible capacity as high as 1,048 mA·h·g^{-1} at 50 mA·g^{-1} and good cycling stability, with a capacity retention of 804 mA·h·g^{-1} after 60 cycles, as well as an outstanding rate performance, with a capacity of 332 mA·h·g^{-1}, achieved even when the electrode was cycled at 3,000 mA·g^{-1} (Figs. 15(a) and 15(b)). Furthermore, when a full cell was assembled using Se_4P_4 as the anode and $Na_3(VO_{0.5})_2(PO_4)_2F_2$/C as the cathode, the cell exhibited a discharge capacity of 985 mA·h·g^{-1} with an average output voltage of about 2.5 V and a capacity retention of 90.6% after 50 cycles. *Ex situ* XRD, TEM, and *in situ* Raman analysis demonstrated that Se_4P_4 is converted into Na_2Se and Na_3P after full discharge and converted to amorphous Se_4P_4 in the subsequent charging process, as illustrated in Fig. 15(c).

Duveau et al. reported that SiP_2 showed potential as an anode for LIBs and SIBs [119]. The ball-milled SiP_2 displayed an initial reversible capacity of 843 mA·h·g^{-1} as an anode for SIBs, although the capacity faded rapidly with only a charge capacity of only 572 mA·h·g^{-1} remaining after 15 cycles.

5 Conclusions and perspectives

Phosphorus and metal phosphides show great advantages as anodes for SIBs because of their unique physical properties and outstanding electrochemical characteristics. Although research on the applications of phosphorus and phosphides to SIBs is just emerging, remarkable progress has been achieved.

Nevertheless, there are still many drawbacks that must be overcome to accelerate the practical application of SIBs. In this review, we have provided a com-

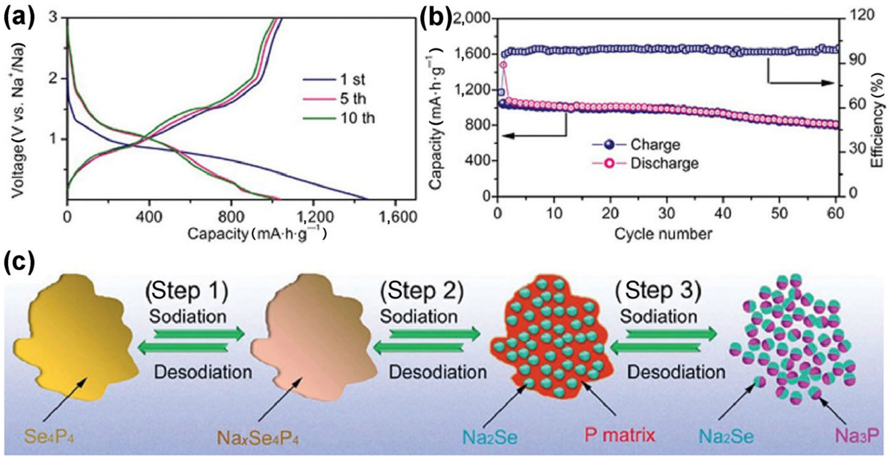

Figure 15 (a) Galvanostatic discharge and charge curves and (b) cycling performance and the corresponding coulombic efficiency of Se_4P_4. (c) Schematic illustration of the mechanism of Se_4P_4 during sodiation/desodiation. Reproduced with permission from Ref. [118], © 2016 WILEY-VCH Verlag GmbH & Co. KGaA, Weinheim.

prehensive overview of recent developments in nanostructured phosphorus and metal phosphides for SIBs.

In the case of phosphorus, huge volumetric expansion and relatively low electronic conductivity are the key issues that hinder the full utilization of its high theoretical capacity. Rationally designed nanoarchitectures, such as composites with conductive and robust matrices, e.g. carbon, graphene, and CNTs, can not only relieve the volume charges to obtain stable cycling performance but also enhance the transfer kinetics of sodium ions and electrons [37, 55, 56, 58]. The mechanical ball-milling method has been extensively applied to the synthesis of P/conductive matrix nanocomposites because of its advantages, such as cost-effectiveness and environmentally friendliness; furthermore, this process can be directly adapted for mass production. In these ball-milled P/carbon matrix composites, however, the mass ratio of carbon is usually ≥30 wt.%, and the electrochemical performance rapidly degrades as the carbon content is reduced [36, 37, 52, 56, 58, 59]; consequently, the high carbon content of the matrix significantly increases the production cost and lowers the energy density of SIBs. Other techniques, such as the vaporization-condensation approach, also have been introduced to prepare P/carbon nanocomposites with unique nanostructures. Compared with the mechanical ball milling method, this synthesis strategy allows the inheritance of the morphology of the carbon matrix and the homogeneous distribution of nanosized P particles [52, 61, 62]. For instance, in the case of MOF-derived microporous carbons, such as CMK-3 and 3D graphene aerogel, the morphologies are maintained after deposition with P nanoparticles, and this remarkably enhances their electrochemical performances. Even so, this strategy faces a similar challenge to that for the mechanical ball milling method, i.e., low P weight content. In addition, the by-product, white P, which is generated during the condensation process, is dangerous and must be washed away using a special organic solvent, complicating the synthesis process. Novel strategies are urgently needed to break through these bottlenecks to obtain high-performance nanocomposites with an acceptable carbon content.

Another serious challenge for P is its low initial coulombic efficiency and corresponding large irreversible capacity loss. Generally, not all the sodium ions intercalated into P during the first discharge process can convert back in the subsequent deintercalation because of the formation of SEI films and side reactions with the electrolyte. Compared with bulk P, nanosized P particles have larger contact surface areas with the electrolyte and suffer more side reactions. A feasible way to overcome this is to fabricate a protective layer on the P particles surface (such as TiO_2, SiO_2, or Al_2O_3,) which could be applied to the above-mentioned P/carbon nanocomposites to modify the electrode surface chemistry and reduce the side reactions. Furthermore, electrolyte additives, such as FEC and vinylene carbonate, have been proven to effectively improve the initial coulombic efficiency and cycling stability [74, 120]. More effort should be devoted to understanding the SEI film formation mechanism and the interface chemistry between the electrode and electrolyte to improve the initial coulombic efficiency.

Concerning metal phosphides, the biggest challenge is the large volume variation during electrochemical reactions. Hybrids of phosphorus and carbonaceous matrixes are effective in accommodating the volumetric expansion [38, 39, 45, 46, 94, 100]; in addition, other matrices, such as phosphorene and zero-strain TiO_2, show promise for overcoming the volume change problems. Generally, the morphology, particle size, and nanostructure of metal phosphides greatly influence the electrochemical performance of anode materials, and specially designed nanoarchitectures, such as core-shell [39], yolk-shell [105], mesoporous structures [95, 98, 99], and binder-free nanowire arrays [51], have had a remarkable impact on alleviating the large volume variation caused by the sodiation/desodiation processes. Other strategies, such as doping with heteroatoms to modify the local electronic structure, may make a difference in relieving the volume variation and improving the kinetic properties.

Until now, most studies investigating metal phosphides as anode materials in SIBs have focused on carbon matrix composites and the fabrication of new nanoarchitectures to buffer the volumetric expansion. Other metal phosphide systems, such as Mn-P, V-P, Mo-P, and Zn-P, should be considered for exploration as novel anode materials for SIBs because some of these have been successfully used in LIBs and achieved good electrochemical performance. Ternary metal phosphides, such as the Fe-Co-P, Fe-Ni-P, and Ni-Co-P systems [121–124], have been extensively utilized in electrochemical catalysis because of their high electrochemical activities, and they can also be considered for utilization in SIBs. In addition, P-rich phosphides, such as SnP_3, FeP_4, NiP_3, and CuP_2, should be given more attention because of their high P content, which suggests a higher theoretical capacity. For instance, NiP_3 shows good capacity retention with a high reversible capacity of 900 $mA\cdot h\cdot g^{-1}$, which is much higher than that of Ni_2P (because a capacity of only ~200 $mA\cdot h\cdot g^{-1}$ can be achieved) when used as the anode for SIBs [105, 109].

Currently, phosphorus and metal phosphides are being investigated for use as anode materials for SIBs, and much remarkable progress has been made in improving their electrochemical performance. In the future, more effort must be made to analyze the Na-storage mechanism and volume change mechanism to exploit the high theoretical capacity fully. Novel synthetic methods and rationally designed nanoarchitectures are very much required to overcome the issues of volumetric variation, poor electrical conductivity, and low initial coulombic efficiency.

Acknowledgements

This work is supported by the National Natural Science Foundation of China (No. 51673157), Australian Renewable Energy Agency (ARENA) Project (No. G00849), and the Australian Research Council (ARC) linkage project (No. LP120200432). Q. X. thanks for funding support from the China Scholarship Council (CSC). The authors would like to thank Dr. Tania Silver and Dingping Cui for critical reading of the paper.

References

[1] Bruce, P. G.; Freunberger, S. A.; Hardwick, L. J.; Tarascon, J. M. Li-O_2 and Li-S batteries with high energy storage. *Nat. Mater.* **2012**, *11*, 19–29.

[2] Armand, M.; Tarascon, J. M. Building better batteries. *Nature* **2008**, *451*, 652–657.

[3] Palacín, M. R.; de Guibert, A. Why do batteries fail? *Science* **2016**, *351*, 1253292.

[4] Dunn, B.; Kamath, H.; Tarascon, J. M. Electrical energy storage for the grid: A battery of choices. *Science* **2011**, *334*, 928–935.

[5] Armstrong, M. J.; O'Dwyer, C.; Macklin, W. J.; Holmes, J. D. Evaluating the performance of nanostructured materials as lithium-ion battery electrodes. *Nano Res*. **2014**, *7*, 1–62.

[6] Balogun, M. S.; Qiu, W. T.; Luo, Y.; Meng, H.; Mai, W. J.; Onasanya, A.; Olaniyi, T. K.; Tong, Y. X. A review of the development of full cell lithium-ion batteries: The impact of nanostructured anode materials. *Nano Res*. **2016**, *9*, 2823–2851.

[7] Guo, X.; Sun, B.; Su, D. W.; Liu, X. X.; Liu, H.; Wang, Y.; Wang, G. X. Recent developments of aprotic lithium-oxygen batteries: Functional materials determine the electrochemical performance. *Sci. Bull*. **2017**, *62*, 442–452.

[8] Yaksic, A.; Tilton, J. E. Using the cumulative availability curve to assess the threat of mineral depletion: The case of lithium. *Resour. Policy* **2009**, *34*, 185–194.

[9] Kim, Y.; Ha, K. H.; Oh, S. M.; Lee, K. T. High-capacity anode materials for sodium-ion batteries. *Chemistry* **2014**, *20*, 11980–11992.

[10] Yabuuchi, N.; Kubota, K.; Dahbi, M.; Komaba, S. Research development on sodium-ion batteries. *Chem. Rev.* **2014**, *114*, 11636–11682.

[11] Kubota, K.; Komaba, S. Review-practical issues and future perspective for Na-ion batteries. *J. Electrochem. Soc.* **2015**, *162*, A2538–A2550.

[12] Kundu, D.; Talaie, E.; Duffort, V.; Nazar, L. F. The emerging chemistry of sodium ion batteries for electrochemical energy storage. *Angew. Chem. Int. Ed.* **2015**, *54*, 3431–3448.

[13] Dahbi, M.; Yabuuchi, N.; Kubota, K.; Tokiwa, K.; Komaba, S. Negative electrodes for Na-ion batteries. *Phys. Chem. Chem. Phys*. **2014**, *16*, 15007–15028.

[14] Wang, L. P.; Yu, L. H.; Wang, X.; Srinivasan, M.; Xu, Z. J. Recent developments in electrode materials for sodium-ion batteries. *J. Mater. Chem. A***2015**, *3*, 9353–9378.

[15] Xiang, X. D.; Zhang, K.; Chen, J. Recent advances and prospects of cathode materials for sodium-ion batteries. *Adv. Mater.* **2015**, *27*, 5343–5364.

[16] Fang, C.; Huang, Y. H.; Zhang, W. X.; Han, J. T.; Deng, Z.; Cao, Y. L.; Yang, H. X. Routes to high energy cathodes of sodium-ion batteries. *Adv. Energy Mater*. **2016**, *6*, 1501727.

[17] Kim, H.; Kim, H.; Ding, Z.; Lee, M. H.; Lim, K.; Yoon, G.; Kang, K. Recent progress in electrode materials for sodium-ion batteries. *Adv. Energy Mater*. **2016**, *6*, 1600943.

[18] Luo, W.; Shen, F.; Bommier, C.; Zhu, H. L.; Ji, X. L.; Hu, L. B. Na-ion battery anodes: Materials and electrochemistry. *Acc. Chem. Res*. **2016**, *49*, 231–240.

[19] Xiao, Y.; Lee, S. H.; Sun, Y. K. The application of metal sulfides in sodium ion batteries. *Adv*. *Energy Mater*. **2016**, *7*, 1601329.

[20] Ponrouch, A.; Marchante, E.; Courty, M.; Tarascon, J. M.; Palacín, M. R. In search of an optimized electrolyte for Na-ion batteries. *Energy Environ*. *Sci*. **2012**, *5*, 8572–8583.

[21] Cao, Y. L.; Xiao, L. F.; Sushko, M. L.; Wang, W.; Schwenzer, B.; Xiao, J.; Nie, Z. M.; Saraf, L. V.; Yang, Z. G.; Liu, J. Sodium ion insertion in hollow carbon nanowires for battery applications. *Nano Lett*. **2012**, *12*, 3783–3787.

[22] Zhang, N.; Liu, Y. C.; Lu, Y. Y.; Han, X. P.; Cheng, F. Y.; Chen, J. Spherical nano-Sb@C composite as a high-rate and ultra-stable anode material for sodium-ion batteries. *Nano Res*. **2015**, *8*, 3384–3393.

[23] Liu, Z. M.; Yu, X. Y.; Lou, X. W.; Paik, U. Sb@C coaxial nanotubes as a superior long-life and high-rate anode for sodium ion batteries. *Energy Environ*. *Sci*. **2016**, *9*, 2314–2318.

[24] Liu, S.; Feng, J. K.; Bian, X. F.; Liu, J.; Xu, H. The morphology-controlled synthesis of a nanoporous-antimony anode for high-performance sodium-ion batteries. *Energy Environ*. *Sci*. **2016**, *9*, 1229–1236.

[25] Li, Z.; Ding, J.; Mitlin, D. Tin and tin compounds for sodium ion battery anodes: Phase transformations and performance. *Acc*. *Chem*. *Res*. **2015**, *48*, 1657–1665.

[26] He, M.; Walter, M.; Kravchyk, K. V.; Erni, R.; Widmer, R.; Kovalenko, M. V. Monodisperse SnSb nanocrystals for Li-ion and Na-ion battery anodes: Synergy and dissonance between Sn and Sb. *Nanoscale* **2015**, *7*, 455–459.

[27] Liu, J.; Yang, Z. Z.; Wang, J. Q.; Gu, L.; Maier, J.; Yu, Y. Three-dimensionally interconnected nickel-antimony intermetallic hollow nanospheres as anode material for high-rate sodium-ion batteries. *Nano Energy* **2015**, *16*, 389–398.

[28] Lee, C. W.; Kim, J. C.; Park, S.; Song, H. J.; Kim, D. W. Highly stable sodium storage in 3-D gradational Sb-NiSb-Ni heterostructures. *Nano Energy* **2015**, *15*, 479–489.

[29] Hou, H. S.; Cao, X. Y.; Yang, Y. C.; Fang, L. B.; Pan, C. C.; Yang, X. M.; Song, W. X.; Ji, X. B. NiSb alloy hollow nanospheres as anode materials for rechargeable lithium ion batteries. *Chem*. *Commun*. **2014**, *50*, 8201–8203.

[30] Dou, Y. H.; Wang, Y. X.; Tian, D. L.; Xu, J. T.; Zhang, Z. J.; Liu, Q. N.; Ruan, B. Y.; Ma, J. M.; Sun, Z. Q.; Dou, S. X. Atomically thin Co_3O_4 nanosheet-coated stainless steel mesh with enhanced capacitive Na^+ storage for high-performance sodium-ion batteries. *2D Mater*. **2017**, *4*, 015022.

[31] Yuan, S.; Huang, X. L.; Ma, D. L.; Wang, H. G.; Meng, F. Z.; Zhang, X. B. Engraving copper foil to give large-scale binder-free porous CuO arrays for a high-performance sodium-ion battery anode. *Adv*. *Mater*. **2014**, *26*, 2273–2279.

[32] Wang, L.; Bi, X. F.; Yang, S. B. Partially single-crystalline mesoporous Nb_2O_5 nanosheets in between graphene for ultrafast sodium storage. *Adv*. *Mater*. **2016**, *28*, 7672–7679.

[33] Zhang, K.; Park, M.; Zhou, L. M.; Lee, G. H.; Shin, J.; Hu, Z.; Chou, S. L.; Chen, J.; Kang, Y. M. Cobalt-doped FeS_2 nanospheres with complete solid solubility as a high-performance anode material for sodium-ion batteries. *Angew*. *Chem*. *Int*. *Ed*. *Engl*. **2016**, *55*, 12822–12826.

[34] Song, X. S.; Li, X. F.; Bai, Z. M.; Yan, B.; Li, D. J.; Sun, X. L. Morphology-dependent performance of nanostructured Ni_3S_2/Ni anode electrodes for high performance sodium ion batteries. *Nano Energy* **2016**, *26*, 533–540.

[35] Yu, D. Y. W.; Prikhodchenko, P. V.; Mason, C. W.; Batabyal, S. K.; Gun, J.; Sladkevich, S.; Medvedev, A. G.; Lev, O. High-capacity antimony sulphide nanoparticle-decorated graphene composite as anode for sodium-ion batteries. *Nat*. *Commun*. **2013**, *4*, 2922.

[36] Qian, J. F.; Wu, X. Y.; Cao, Y. L.; Ai, X. P.; Yang, H. X. High capacity and rate capability of amorphous phosphorus for sodium ion batteries. *Angew*. *Chem*. *Int*. *Ed*. *Engl*. **2013**, *52*, 4633–4636.

[37] Kim, Y.; Park, Y.; Choi, A.; Choi, N. S.; Kim, J.; Lee, J.; Ryu, J. H.; Oh, S. M.; Lee, K. T. An amorphous red phosphorus/carbon composite as a promising anode material for sodium ion batteries. *Adv*. *Mater*. **2013**, *25*, 3045–3049.

[38] Qian, J. F.; Xiong, Y.; Cao, Y. L.; Ai, X. P.; Yang, H. X. Synergistic Na-storage reactions in Sn_4P_3 as a high-capacity, cycle-stable anode of Na-ion batteries. *Nano Lett*. **2014**, *14*, 1865–1869.

[39] Li, W. J.; Chou, S. L.; Wang, J. Z.; Kim, J. H.; Liu, H. K.; Dou, S. X. $Sn_{4+x}P_3$@Amorphous Sn-P composites as anodes for sodium-ion batteries with low cost, high capacity, long life, and superior rate capability. *Adv*. *Mater*. **2014**, *26*, 4037–4042.

[40] Kim, Y.; Kim, Y.; Choi, A.; Woo, S.; Mok, D.; Choi, N. S.; Jung, Y. S.; Ryu, J. H.; Oh, S. M.; Lee, K. T. Tin phosphide as a promising anode material for Na-ion batteries. *Adv*. *Mater*. **2014**, *26*, 4139–4144.

[41] Park, C. M.; Sohn, H. J. Black phosphorus and its composite for lithium rechargeable batteries. *Adv*. *Mater*. **2007**, *19*, 2465–2468.

[42] Wang, L.; He, X. M.; Li, J. J.; Sun, W. T.; Gao, J.; Guo, J. W.; Jiang, C. Y. Nano-structured phosphorus composite as high-capacity anode materials for lithium batteries. *Angew*. *Chem*. *Int*. *Ed*. *Engl*. **2012**, *51*, 9034–9037.

[43] Qian, J. F.; Qiao, D.; Ai, X. P.; Cao, Y. L.; Yang, H. X. Reversible 3-Li storage reactions of amorphous phosphorus as high capacity and cycling-stable anodes for Li-ion batteries. *Chem*. *Commun*. **2012**, *48*, 8931–8933.

[44] Sun, J.; Lee, H. W.; Pasta, M.; Yuan, H. T.; Zheng, G. Y.; Sun, Y. M.; Li, Y. Z.; Cui, Y. A phosphorene-graphene

hybrid material as a high-capacity anode for sodium-ion batteries. *Nat. Nanotechnol.* **2015**, *10*, 980–985.

[45] Li, W. J.; Chou, S. L.; Wang, J. Z.; Liu, H. K.; Dou, S. X. A new, cheap, and productive FeP anode material for sodium-ion batteries. *Chem. Commun.* **2015**, *51*, 3682–3685.

[46] Yang, Q. R.; Li, W. J.; Chou, S. L.; Wang, J. Z.; Liu, H. K. Ball-milled FeP/graphite as a low-cost anode material for the sodium-ion battery. *RSC Adv.* **2015**, *5*, 80536–80541.

[47] Li, W. J.; Yang, Q. R.; Chou, S. L.; Wang, J. Z.; Liu, H. K. Cobalt phosphide as a new anode material for sodium storage. *J. Power Sources* **2015**, *294*, 627–632.

[48] Lu, J.; Chen, Z. H.; Ma, Z. F.; Pan, F.; Curtiss, L. A.; Amine, K. The role of nanotechnology in the development of battery materials for electric vehicles. *Nat. Nanotechnol.* **2016**, *11*, 1031–1038.

[49] Zhao, Y.; Li, X. F.; Yan, B.; Xiong, D. B.; Li, D. J.; Lawes, S.; Sun, X. L. Recent developments and understanding of novel mixed transition-metal oxides as anodes in lithium ion batteries. *Adv. Energy Mater.* **2016**, *6*, 1502175.

[50] Liu, J.; Kopold, P.; Wu, C.; van Aken, P. A.; Maier, J.; Yu, Y. Uniform yolk–shell Sn_4P_3@C nanospheres as high-capacity and cycle-stable anode materials for sodium-ion batteries. *Energy Environ. Sci.* **2015**, *8*, 3531–3538.

[51] Fan, M. P.; Chen, Y.; Xie, Y. H.; Yang, T. Z.; Shen, X. W.; Xu, N.; Yu, H. Y.; Yan, C. L. Half-cell and full-cell applications of highly stable and binder-free sodium ion batteries based on Cu_3P nanowire anodes. *Adv. Funct. Mater.* **2016**, *26*, 5019–5027.

[52] Gao, H.; Zhou, T. F.; Zheng, Y.; Liu, Y. Q.; Chen, J.; Liu, H. K.; Guo, Z. P. Integrated carbon/red phosphorus/graphene aerogel 3D architecture via advanced vapor-redistribution for high-energy sodium-ion batteries. *Adv. Energy Mater.* **2016**, *6*, 1601037.

[53] Pei, L. K.; Zhao, Q.; Chen, C. C.; Liang, J.; Chen, J. Phosphorus nanoparticles encapsulated in graphene scrolls as a high-performance anode for sodium-ion batteries. *ChemElectroChem* **2015**, *2*, 1652–1655.

[54] Lee, G.-H.; Jo, M. R.; Zhang, K.; Kang, Y. M. A reduced graphene oxide-encapsulated phosphorus/carbon composite as a promising anode material for high-performance sodium-ion batteries. *J. Mater. Chem. A* **2017**, *5*, 3683–3690.

[55] Li, W. J.; Chou, S. L.; Wang, J. Z.; Liu, H. K.; Dou, S. X. Significant enhancement of the cycling performance and rate capability of the P/C composite *via* chemical bonding (P-C). *J. Mater. Chem. A* **2016**, *4*, 505–511.

[56] Song, J. X.; Yu, Z. X.; Gordin, M. L.; Hu, S.; Yi, R.; Tang, D. H.; Walter, T.; Regula, M.; Choi, D.; Li, X. L. et al. Chemically bonded phosphorus/graphene hybrid as a high performance anode for sodium-ion batteries. *Nano Lett.* **2014**, *14*, 6329–6335.

[57] Zhu, Y. J.; Wen, Y.; Fan, X. L.; Gao, T.; Han, F. D.; Luo, C.; Liou, S. C.; Wang, C. S. Red phosphorus-single-walled carbon nanotube composite as a superior anode for sodium ion batteries. *ACS Nano* **2015**, *9*, 3254–3264.

[58] Song, J. X.; Yu, Z. X.; Gordin, M. L.; Li, X. L.; Peng, H. S.; Wang, D. H. Advanced sodium ion battery anode constructed *via* chemical bonding between phosphorus, carbon nanotube, and cross-linked polymer binder. *ACS Nano* **2015**, *9*, 11933–11941.

[59] Li, W. J.; Chou, S. L.; Wang, J. Z.; Liu, H. K.; Dou, S. X. Simply mixed commercial red phosphorus and carbon nanotube composite with exceptionally reversible sodium-ion storage. *Nano Lett.* **2013**, *13*, 5480–5484.

[60] Li, M. Y.; Carter, R.; Oakes, L.; Douglas, A.; Muralidharan, N.; Pint, C. L. Role of carbon defects in the reversible alloying states of red phosphorus composite anodes for efficient sodium ion batteries. *J.Mater. Chem. A***2017**, *5*, 5266–5272.

[61] Li, W. H.; Yang, Z. Z.; Li, M. S.; Jiang, Y.; Wei, X.; Zhong, X. W.; Gu, L.; Yu, Y. Amorphous red phosphorus embedded in highly ordered mesoporous carbon with superior lithium and sodium storage capacity. *Nano Lett.* **2016**, *16*, 1546–1553.

[62] Li, W. H.; Hu, S. H.; Luo, X. Y.; Li, Z. L.; Sun, X. Z.; Li, M. S.; Liu, F. F.; Yu, Y. Confined amorphous red phosphorus in MOF-derived N-doped microporous carbon as a superior anode for sodium-ion battery. *Adv. Mater.* **2017**, *29*, 1605820.

[63] Kim, S. O.; Manthiram, A. High-performance red P-based P-TiP_2-C nanocomposite anode for lithium-ion and sodium-ion storage. *Chem. Mater.* **2016**, *28*, 5935–5942.

[64] Walter, M.; Erni, R.; Kovalenko, M. V. Inexpensive antimony nanocrystals and their composites with red phosphorus as high-performance anode materials for Na-ion batteries. *Sci. Rep.* **2015**, *5*, 8418.

[65] Eswaraiah, V.; Zeng, Q. S.; Long, Y.; Liu, Z. Black phosphorus nanosheets: Synthesis, characterization and applications. *Small* **2016**, *12*, 3480–3502.

[66] Batmunkh, M.; Bat-Erdene, M.; Shapter, J. G. Phosphorene and phosphorene-based materials-prospects for future applications. *Adv. Mater.* **2016**, *28*, 8586–8617.

[67] Du, Y. L.; Ouyang, C. Y.; Shi, S. Q.; Lei, M. S. Ab initio studies on atomic and electronic structures of black phosphorus. *J. Appl. Phys.* **2010**, *107*, 093718.

[68] Liu, H.; Du, Y. C.; Deng, Y. X.; Ye, P. D. Semiconducting black phosphorus: Synthesis, transport properties and electronic applications. *Chem. Soc. Rev.* **2015**, *44*, 2732–2743.

[69] Bacon, G. E. The interlayer spacing of graphite. *Acta Crystallogr.* **1951**, *4*, 558–561.

[70] Morita, A. Semiconducting black phosphorus. *Appl. Phys. A* **1986**, *39*, 227–242.

[71] Hultgren, R.; Gingrich, N. S.; Warren, B. E. The atomic distribution in red and black phosphorus and the crystal structure of black phosphorus. *J. Chem. Phys.* **1935**, *3*, 351–355.

[72] Xu, G. L.; Chen, Z. H.; Zhong, G. M.; Liu, Y. Z.; Yang, Y.; Ma, T. Y.; Ren, Y.; Zuo, X. B.; Wu, X. H.; Zhang, X. Y. et al. Nanostructured black phosphorus/ketjenblack-multiwalled carbon nanotubes composite as high performance anode material for sodium-ion batteries. *Nano Lett.* **2016**, *16*, 3955–3965.

[73] Sun, J.; Zheng, G. Y.; Lee, H. W.; Liu, N.; Wang, H. T.; Yao, H. B.; Yang, W. S.; Cui, Y. Formation of stable phosphorus–carbon bond for enhanced performance in black phosphorus nanoparticle-graphite composite battery anodes. *Nano Lett.* **2014**, *14*, 4573–4580.

[74] Dahbi, M.; Yabuuchi, N.; Fukunishi, M.; Kubota, K.; Chihara, K.; Tokiwa, K.; Yu, X. F.; Ushiyama, H.; Yamashita, K.; Son, J. Y. et al. Black phosphorus as a high-capacity, high-capability negative electrode for sodium-ion batteries: Investigation of the electrode/electrolyte interface. *Chem. Mater.* **2016**, *28*, 1625–1635.

[75] Hembram, K. P. S. S.; Jung, H.; Yeo, B. C.; Pai, S. J.; Kim, S.; Lee, K. R.; Han, S. S. Unraveling the atomistic sodiation mechanism of black phosphorus for sodium ion batteries by first-principles calculations. *J. Phys. Chem. C* **2015**, *119*, 15041–15046.

[76] Hembram, K. P. S. S.; Jung, H.; Yeo, B. C.; Pai, S. J.; Lee, H. J.; Lee, K. R.; Han, S. S. A comparative first-principles study of the lithiation, sodiation, and magnesiation of black phosphorus for Li-, Na-, and Mg-ion batteries. *Phys. Chem. Chem. Phys.* **2016**, *18*, 21391–21397.

[77] Ramireddy, T.; Xing, T.; Rahman, M. M.; Chen, Y.; Dutercq, Q.; Gunzelmann, D.; Glushenkov, A. M. Phosphorus-carbon nanocomposite anodes for lithium-ion and sodium-ion batteries. *J. Mater. Chem. A* **2015**, *3*, 5572–5584.

[78] Shi, L.; Zhao, T. S. Recent advances in inorganic 2D materials and their applications in lithium and sodium batteries. *J. Mater. Chem. A* **2017**, *5*, 3735–3758.

[79] Du, H. W.; Lin, X.; Xu, Z. M.; Chu, D. W. Recent developments in black phosphorus transistors. *J. Mater. Chem. C* **2015**, *3*, 8760–8775.

[80] Liu, X.; Wen, Y. W.; Chen, Z. Z.; Shan, B.; Chen, R. A first-principles study of sodium adsorption and diffusion on phosphorene. *Phys. Chem. Chem. Phys.* **2015**, *17*, 16398–16404.

[81] Kulish, V. V.; Malyi, O. I.; Persson, C.; Wu, P. Phosphorene as an anode material for Na-ion batteries: A first-principles study. *Phys. Chem. Chem. Phys.* **2015**, *17*, 13921–13928.

[82] Tran, V.; Soklaski, R.; Liang, Y. F.; Yang, L. Layer-controlled band gap and anisotropic excitons in few-layer black phosphorus. *Phys. Rev. B* **2014**, *89*, 235319.

[83] Takao, Y.; Asahina, H.; Morita, A. Electronic structure of black phosphorus in tight binding approach. *J. Phys. Soc. Jpn.* **1981**, *50*, 3362–3369.

[84] Liu, H.; Neal, A. T.; Zhu, Z.; Luo, Z.; Xu, X. F.; Tománek, D.; Ye, P. D. Phosphorene: An unexplored 2D semiconductor with a high hole mobility. *ACS Nano* **2014**, *8*, 4033–4041.

[85] Li, L. K.; Yu, Y. J.; Ye, G. J.; Ge, Q. Q.; Ou, X. D.; Wu, H.; Feng, D. L.; Chen, X. H.; Zhang, Y. B. Black phosphorus field-effect transistors. *Nat. Nanotechnol.* **2014**, *9*, 372–377.

[86] Engel, M.; Steiner, M.; Avouris, P. Black phosphorus photodetector for multispectral, high-resolution imaging. *Nano Lett.* **2014**, *14*, 6414–6417.

[87] Qiao, J. S.; Kong, X. H.; Hu, Z. X.; Yang, F.; Ji, W. High-mobility transport anisotropy and linear dichroism in few-layer black phosphorus. *Nat. Commun.* **2014**, *5*, 4475.

[88] Yuan, H. T.; Liu, X. G.; Afshinmanesh, F.; Li, W.; Xu, G.; Sun, J.; Lian, B.; Curto, A. G.; Ye, G. J.; Hikita, Y. et al. Polarization-sensitive broadband photodetector using a black phosphorus vertical p-n junction. *Nat. Nanotechnol.* **2015**, *10*, 707–713.

[89] Dai, J.; Zeng, X. C. Bilayer phosphorene: Effect of stacking order on bandgap and its potential applications in thin-film solar cells. *J. Phys. Chem. Lett.* **2014**, *5*, 1289–1293.

[90] Yang, J.; Xu, R. J.; Pei, J. J.; Myint, Y. W.; Wang, F.; Wang, Z.; Zhang, S.; Yu, Z. F.; Lu, Y. R. Optical tuning of exciton and trion emissions in monolayer phosphorene. *Light Sci. Appl.* **2015**, *4*, e312.

[91] Li, W. F.; Yang, Y. M.; Zhang, G.; Zhang, Y. W. Ultrafast and directional diffusion of lithium in phosphorene for high-performance lithium-ion battery. *Nano Lett.* **2015**, *15*,1691–1697.

[92] Zhang, Y.; Wang, H. W.; Luo, Z. Z.; Tan, H. T.; Li, B.; Sun, S. N.; Li, Z.; Zong, Y.; Xu, Z. J.; Yang, Y. H. et al. An air-stable densely packed phosphorene-graphene composite toward advanced lithium storage properties. *Adv. Energy Mater.* **2016**, *6*, 1600453.

[93] Nie, A. M.; Cheng, Y. C.; Ning, S. C.; Foroozan, T.; Yasaei, P.; Li, W.; Song, B. A.; Yuan, Y. F.; Chen, L.; Salehi-Khojin, A. et al. Selective ionic transport pathways in phosphorene. *Nano Lett.* **2016**, *16*, 2240–2247.

[94] Li, Q.; Li, Z. Q.; Zhang, Z. W.; Li, C. X.; Ma, J. Y.; Wang, C. X.; Ge, X. L.; Dong, S. H.; Yin, L. W. Low-temperature solution-based phosphorization reaction route to Sn_4P_3/reduced graphene oxide nanohybrids as anodes for sodium ion batteries. *Adv. Energy Mater.* **2016**, *6*, 1600376.

[95] Han, F.; Tan, C. Y. J.; Gao, Z. Q. Improving the specific capacity and cyclability of sodium-ion batteries by engineering a dual-carbon phase-modified amorphous and mesoporous iron phosphide. *ChemElectroChem* **2016**, *3*, 1054–1062.

[96] Zhang, W. J.; Dahbi, M.; Amagasa, S.; Yamada, Y.; Komaba, S. Iron phosphide as negative electrode material for Na-ion batteries. *Electrochem*. *Commun*. **2016**, *69*, 11–14.

[97] Guo, G. L.; Guo, Y. Y.; Tan, H. T.; Yu, H.; Chen, W. H.; Fong, E. L.; Yan, Q. Y. From fibrous elastin proteins to one-dimensional transition metal phosphides and their applications. *J. Mater*. *Chem*. *A* **2016**, *4*, 10893–10899.

[98] Ge, X. L.; Li, Z. Q.; Yin, L. W. Metal-organic frameworks derived porous core/shell CoP@C polyhedrons anchored on 3D reduced graphene oxide networks as anode for sodium-ion battery. *Nano Energy* **2017**, *32*, 117–124.

[99] Li, Z. Q.; Zhang, L. Y.; Ge, X. L.; Li, C. X.; Dong, S. H.; Wang, C. X.; Yin, L. W. Core–shell structured CoP/FeP porous microcubes interconnected by reduced graphene oxide as high performance anodes for sodium ion batteries. *Nano Energy* **2017**, *32*, 494–502.

[100] Zhao, F. P.; Han, N.; Huang, W. J.; Li, J. J.; Ye, H. L.; Chen, F. J.; Li, Y. G. Nanostructured CuP_2/C composites as high- performance anode materials for sodium ion batteries. *J. Mater*. *Chem*. *A* **2015**, *3*, 21754–21759.

[101] Kim, S. O.; Manthiram, A. The facile synthesis and enhanced sodium-storage performance of a chemically bonded CuP_2/C hybrid anode. *Chem*. *Commun*. **2016**, *52*, 4337–4340.

[102] Komaba, S.; Murata, W.; Ishikawa, T.; Yabuuchi, N.; Ozeki, T.; Nakayama, T.; Ogata, A.; Gotoh, K.; Fujiwara, K. Electrochemical Na insertion and solid electrolyte interphase for hard-carbon electrodes and application to Na-ion batteries. *Adv*. *Funct*. *Mater*. **2011**, *21*, 3859–3867.

[103] Ponrouch, A.; Goñi, A. R.; Palacín, M. R. High capacity hard carbon anodes for sodium ion batteries in additive free electrolyte. *Electrochem*. *Commun*. **2013**, *27*, 85–88.

[104] Zhang, X. Q.; Li, X. N.; Liang, J. W.; Zhu, Y. C.; Qian, Y. T. Synthesis of MoS_2@C nanotubes via the kirkendall effect with enhanced electrochemical performance for lithium ion and sodium ion batteries. *Small* **2016**, *12*, 2484–2491.

[105] Wu, C.; Kopold, P.; van Aken, P. A.; Maier, J.; Yu, Y. High performance graphene/Ni_2P hybrid anodes for lithium and sodium storage through 3D yolk–shell-like nanostructural design. *Adv*. *Mater*. **2017**, *29*, 1604015.

[106] Fan, X. L.; Mao, J. F.; Zhu, Y. J.; Luo, C.; Suo, L. M.; Gao, T.; Han, F. D.; Liou, S. C.; Wang, C. S. Superior stable self-healing SnP_3 anode for sodium-ion batteries. *Adv*. *Energy Mater*. **2015**, *5*, 1500174.

[107] Usui, H.; Sakata, T.; Shimizu, M.; Sakaguchi, H. Electrochemical Na-insertion/extraction properties of Sn-P anodes. *Electrochemistry* **2015**, *83*, 810–812.

[108] Zheng, L. T.; Dunlap, R. A.; Obrovac, M. N. The electrochemical reaction mechanism of tin phosphide with sodium. *J. Electrochem*. *Soc*. **2016**, *163*, A1188–A1191.

[109] Fullenwarth, J.; Darwiche, A.; Soares, A.; Donnadieu, B.; Monconduit, L. NiP_3: A promising negative electrode for Li- and Na-ion batteries. *J. Mater*. *Chem*. *A* **2014**, *2*, 2050–2059.

[110] Liu, S. L.; Zhang, H. Z.; Xu, L. Q.; Ma, L. B.; Chen, X. X. Solvothermal preparation of tin phosphide as a long-life anode for advanced lithium and sodium ion batteries. *J. Power Sources* **2016**, *304*, 346–353.

[111] Shin, H. S.; Jung, K. N.; Jo, Y. N.; Park, M. S.; Kim, H.; Lee, J. W. Tin phosphide-based anodes for sodium-ion batteries: Synthesis via solvothermal transformation of Sn metal and phase-dependent Na storage performance. *Sci*. *Rep*. **2016**, *6*, 26195.

[112] Seh, Z. W.; Li, W. Y.; Cha, J. J.; Zheng, G. Y.; Yang, Y.; McDowell, M. T.; Hsu, P. C.; Cui, Y. Sulphur-TiO_2 yolk–shell nanoarchitecture with internal void space for long-cycle lithium-sulphur batteries. *Nat*. *Commun*. **2013**, *4*, 1331.

[113] Liu, N.; Wu, H.; McDowell, M. T.; Yao, Y.; Wang, C. M.; Cui, Y. A yolk–shell design for stabilized and scalable Li-ion battery alloy anodes. *Nano Lett*. **2012**, *12*, 3315–3321.

[114] Hong, Y. J.; Son, M. Y.; Kang, Y. C. One-pot facile synthesis of double-shelled SnO_2 yolk–shell-structured powders by continuous process as anode materials for Li-ion batteries. *Adv*. *Mater*. **2013**, *25*, 2279–2283.

[115] Wang, Y. X.; Yang, J. P.; Chou, S. L.; Liu, H. K.; Zhang, W. X.; Zhao, D. Y.; Dou, S. X. Uniform yolk–shell iron sulfide-carbon nanospheres for superior sodium-iron sulfide batteries. *Nat*. *Commun*. **2015**, *6*, 8689.

[116] Liu, N.; Lu, Z. D.; Zhao, J.; McDowell, M. T.; Lee, H. W.; Zhao, W. T.; Cui, Y. A pomegranate-inspired nanoscale design for large-volume-change lithium battery anodes. *Nat*. *Nanotechnol*. **2014**, *9*, 187–192.

[117] Hall, J. W.; Membreno, N.; Wu, J.; Celio, H.; Jones, R. A.; Stevenson, K. J. Low-temperature synthesis of amorphous FeP_2 and its use as anodes for Li ion batteries. *J. Am*. *Chem*. *Soc*. **2012**, *134*, 5532–5535.

[118] Lu, Y. Y.; Zhou, P. F.; Lei, K. X.; Zhao, Q.; Tao, Z. L.; Chen, J. Selenium phosphide (Se_4P_4) as a new and promising anode material for sodium-ion batteries. *Adv*. *Energy Mater*. **2017**, *7*, 1601973.

[119] Duveau, D.; Israel, S. S.; Fullenwarth, J.; Cunin, F.; Monconduit, L. Pioneer study of SiP_2 as negative electrode for Li- and Na-ion batteries. *J. Mater*. *Chem*. *A* **2016**, *4*, 3228–3232.

[120] Yabuuchi, N.; Matsuura, Y.; Ishikawa, T.; Kuze, S.; Son, J. Y.; Cui, Y. T.; Oji, H.; Komaba, S. Phosphorus electrodes in sodium cells: Small volume expansion by sodiation and the surface-stabilization mechanism in aprotic solvent. *ChemElectroChem* **2014**, *1*, 580–589.

[121] Shi, Y. M.; Zhang, B. Recent advances in transition metal phosphide nanomaterials: Synthesis and applications in hydrogen evolution reaction. *Chem*. *Soc*. *Rev*. **2016**, *45*, 1529–1541.

[122] Tang, C.; Gan, L. F.; Zhang, R.; Lu, W. B.; Jiang, X. E.; Asiri, A. M.; Sun, X. P.; Wang, J.; Chen, L. Ternary $Fe_xCo_{1-x}P$ nanowire array as a robust hydrogen evolution reaction electrocatalyst with Pt-like activity: Experimental and theoretical insight. *Nano Lett*. **2016**, *16*, 6617–6621.

[123] Tang, C.; Zhang, R.; Lu, W. B.; He, L. B.; Jiang, X. E.; Asiri, A. M.; Sun, X. P. Fe-doped CoP nanoarray: A monolithic multifunctional catalyst for highly efficient hydrogen generation. *Adv*. *Mater*. **2017**, *29*, 1602441.

[124] Gong, M.; Dai, H. J. A mini review of NiFe-based materials as highly active oxygen evolution reaction electrocatalysts. *Nano Res*. **2015**, *8*, 23–39.